



HAL
open science

Phase driven study for stochastic linear multi-dofs dynamic response

Emmanuelle Sarrouy

► **To cite this version:**

Emmanuelle Sarrouy. Phase driven study for stochastic linear multi-dofs dynamic response. Mechanical Systems and Signal Processing, 2019, 10.1016/j.ymssp.2019.04.042 . hal-02120580

HAL Id: hal-02120580

<https://hal.science/hal-02120580>

Submitted on 9 Dec 2019

HAL is a multi-disciplinary open access archive for the deposit and dissemination of scientific research documents, whether they are published or not. The documents may come from teaching and research institutions in France or abroad, or from public or private research centers.

L'archive ouverte pluridisciplinaire **HAL**, est destinée au dépôt et à la diffusion de documents scientifiques de niveau recherche, publiés ou non, émanant des établissements d'enseignement et de recherche français ou étrangers, des laboratoires publics ou privés.

Phase driven study for stochastic linear multi-dofs dynamic response

E. Sarrouy^{a,*}

^a*Aix Marseille Univ, CNRS, Centrale Marseille, LMA, Marseille, France*

Abstract

This work addresses the computation of dynamic responses of stochastic linear systems using polynomial chaos expansion. As is now well known, polynomial chaos does not offer an accurate representation of dynamic response around resonances when the responses are evaluated for several frequency values. A new parametrization of the frequency response function is then proposed: instead of considering the frequency as the main parameter, a “total phase” parameter is defined and used to define the dynamical system to be solved. It is shown via two applications that this approach offers very accurate results when conjugated to polynomial chaos with low degree.

Keywords: Structural dynamics, Uncertainty, Polynomial Chaos, Frequency response function

1. Introduction

Evaluation of the frequency response function (frf) is one of the main steps of a study in the frame of structural dynamics. In the case of deterministic linear systems, this presents no major difficulty except for the computational cost
5 when processing large systems. However, when uncertainties are introduced the robust Monte Carlo Simulation (MCS) method leads to prohibitive computational costs. Hence, several works propose to overcome this problem by using different approaches: building surrogate mode-based models [1], Kriging [2] or polynomial chaos for example. In this latter case, multiple studies showed that
10 for stochastic systems, the classical generalized Polynomial Chaos (gPC, [3]) fails to offer an accurate representation of the stochastic dynamic response in the vicinity of resonances, that is in frequency ranges where accuracy is especially required. This phenomenon is emphasized over a single degree of freedom (dof) in [4] and in the frame of rotor dynamics in [5]. It is analysed in [6] as
15 “PC-resonances” that is resonances due to Polynomial Chaos Expansion (PCE) which are located close to the dynamical system resonances.

*Corresponding author. Tel.: +33 484 524 264.

Email address: emmanuelle.sarrouy@centrale-marseille.fr (E. Sarrouy)

To overcome this problem, [Jacquelin et al.](#) proposed to use an accelerating scheme to get faster convergence of PCE for the first two moments [7]; Multi-Element generalized Polynomial Chaos method [8] can also be applied successfully as tested in [4]. Another possibility is to use another parametrization of the frf as proposed in [9] for a single dof system: instead of computing the dynamic stochastic responses for different frequencies, the stochastic responses are evaluated for different response phase values; this leads to a simpler dependency of the response with respect to the random variables and hence a more accurate representation using low degree polynomials. This work is a generalization of this phase parametrization approach to linear systems with multiple dofs. It is close to a recent work by [Yaghoubi et al.](#) who propose a piecewise linear transform of frequency intervals between several selected frequencies (resonances and anti-resonance) [10]. This work proposes an analytic function instead of a two steps process (frequencies selection and piecewise linear transformations). Considering multiple dofs, a “total phase” parameter is defined and the stochastic dynamical problem formulation is redefined accordingly. The idea is that for a same value of the scalar “total phase” different realizations will have close responses which will be accurately represented using low degree polynomials whereas for a same frequency value, the responses from one realization to another can be very different and hence require higher degree polynomials.

The theoretical steps are detailed in Sec. 2. Sec. 3 is devoted to computational considerations and defines an approximate expression of the “total phase” which can save time for large systems. Finally, the classical approach and the proposed one are compared via two numerical applications in Sec. 4.

2. Problem statement and theoretical points

Let’s consider a general linear damped multi-dofs system in its classical formulation:

$$\mathbf{M}\ddot{\mathbf{u}} + \mathbf{C}\dot{\mathbf{u}} + \mathbf{K}\mathbf{u} = \mathbf{f}(t) \quad (1)$$

This is a second order linear ordinary differential equation with constant coefficients; let us denote its size n . It is assumed throughout the paper that the mass and stiffness matrices \mathbf{M} and \mathbf{K} are symmetric definite positive and that the damping matrix \mathbf{C} is such that it reflects a sub-critical damping. When working in the field of structural dynamics, one usually wants to establish the frf of system (1). The excitation $\mathbf{f}(t)$ is assumed to be periodic with a single frequency component:

$$\mathbf{f}(t) = \mathbf{f}^c \cos(\omega t) + \mathbf{f}^s \sin(\omega t), \quad (\mathbf{f}^c, \mathbf{f}^s) \in (\mathbb{R}^n)^2 \quad (2)$$

The stationary response \mathbf{u} is then sought in a similar form:

$$\mathbf{u}(t) = \mathbf{a} \cos(\omega t) + \mathbf{b} \sin(\omega t), \quad (\mathbf{a}, \mathbf{b}) \in (\mathbb{R}^n)^2 \quad (3)$$

Components \mathbf{a} and \mathbf{b} can be evaluated using a complex reformulation of equation (1) as described in [Appendix A](#):

$$\hat{\mathbf{K}}(\omega)\hat{\mathbf{u}} = \hat{\mathbf{f}} \text{ with } \hat{\mathbf{K}}(\omega) = \mathbf{K} - \omega^2\mathbf{M} + j\omega\mathbf{C} \quad (4)$$

55 where $j^2 = -1$, $\hat{\mathbf{u}} = \mathbf{a} - j\mathbf{b} \in \mathbb{C}^n$ and $\hat{\mathbf{f}} = \mathbf{f}^c - j\mathbf{f}^s \in \mathbb{C}^n$.
 To build a frf, $\hat{\mathbf{u}}$ is evaluated for a given range of circular frequency ω values; to be more specific, it is evaluated for N discrete values $\omega^{(j)}$, $1 \leq j \leq N$ over the range of interest. It is assumed here that the system is damped so that the dynamical flexibility matrix $\hat{\mathbf{S}}(\omega) = \hat{\mathbf{K}}(\omega)^{-1}$ always exists (there are no undamped modes).
 60 Hence, for each circular frequency value ω there is one and only one stationary solution expressed in its complex description $\hat{\mathbf{u}}$ satisfying (1).

Let's now consider uncertainties that are modelled in the probabilistic frame: random variables or random fields are used to render observed or assumed variations of the structure; the excitation vector \mathbf{f} is considered free of any uncertainty.
 65 In the case of random fields, it is assumed here that they are approximated by a collection of uncorrelated random variables via a Karhunen-Loève decomposition [11, 12] for example. Hence uncertainties are eventually rendered via a set of \tilde{n} random variables, denoted ξ_i , $1 \leq i \leq \tilde{n}$. This leads to random matrices and system response which are denoted as follows:
 70

$$\tilde{\mathbf{M}}\ddot{\tilde{\mathbf{u}}} + \tilde{\mathbf{C}}\dot{\tilde{\mathbf{u}}} + \tilde{\mathbf{K}}\tilde{\mathbf{u}} = \mathbf{f}(t) \quad (5)$$

To establish the frf in the stochastic context, the deterministic approach is usually expanded: for several values of ω within the frequency range of interest, $\tilde{\mathbf{u}}$ is evaluated, most frequently in its complex description $\tilde{\hat{\mathbf{u}}}$ as exposed above. The system which is solved is then:

$$\tilde{\hat{\mathbf{K}}}(\omega)\tilde{\hat{\mathbf{u}}} = \hat{\mathbf{f}} \text{ with } \tilde{\hat{\mathbf{K}}}(\omega) = \tilde{\mathbf{K}} - \omega^2\tilde{\mathbf{M}} + j\omega\tilde{\mathbf{C}} \quad (6)$$

75 A way to express $\tilde{\hat{\mathbf{u}}}$ is to expand it into a truncated polynomial series: this is what gPC does [3, 13, 14]. However, it was demonstrated that this representation is non accurate in the vicinity of resonances which are the frequency ranges of interest [4, 5].

The idea developed in this work to overcome such a problem is to read Eq. (4) as n relationships between $n + 1$ variables \hat{u}_k , $1 \leq k \leq n$ (components of $\hat{\mathbf{u}}$) and ω . The classical way to process this dynamical system is formalized as the addition of an $(n + 1)$ -th equation $C(\hat{\mathbf{u}}, \omega) = 0$ where $C(\hat{\mathbf{u}}, \omega) = \omega - \omega^{(j)}$ with $\omega^{(j)}$ a given circular frequency.
 80

We propose to modify this latest equation so as to draw smoother surfaces considering ξ_i variations in the random case, and hence getting a better convergence rate of the gPC for this new problem. First, this new constraint equation is defined based on the modal properties of system (1). Then, its combination with gPC is exposed. A last subsection explains how to get classical – for constant frequencies – results from results of the proposed approach.
 85

90 *2.1. Quadratic eigenvalue problem and total phase definition*

Let's consider the quadratic eigenvalue problem (QEP) associated with Eq. (1):

$$(\lambda_k^2 \mathbf{M} + \lambda_k \mathbf{C} + \mathbf{K}) \boldsymbol{\varphi}_k = \mathbf{0} \quad (7)$$

where λ_k and $\boldsymbol{\varphi}_k$, $1 \leq k \leq 2n$, denote the eigenvalues and eigenvectors respectively.

95 When there is no damping ($\mathbf{C} = \mathbf{0}$), the spectral theorem provides the existence of a basis of real eigenvectors that simultaneously diagonalize \mathbf{M} and \mathbf{K} matrices. For classically damped systems, that is systems with a damping matrix verifying the Caughey condition [15]

$$\mathbf{C} \mathbf{M}^{-1} \mathbf{K} = \mathbf{K} \mathbf{M}^{-1} \mathbf{C} \quad (8)$$

the set of real eigenvectors obtained for the undamped system also diagonalize 100 \mathbf{C} . The eigenvalue problem of non-classically damped systems is not as simple as the two cases mentioned above [16, 17]. In this latter case, there does not always exist a basis (even a complex one) which simultaneously diagonalize mass, damping and stiffness matrices [18, Sec. 1-4].

It is assumed in the rest of the paper that the QEP (7) has $2n$ distinct 105 eigenvalues which are complex (not purely real nor purely imaginary): each mode is damped, none is critically or overdamped. In the case of complex eigenvalues, as matrices are real, if $(\lambda_k, \boldsymbol{\varphi}_k)$ is a solution, then $(\overline{\lambda}_k, \overline{\boldsymbol{\varphi}_k})$ is also a solution: eigenvalues come in complex pairs. Each eigenvalue λ_k can be split into real and imaginary contributions:

$$\lambda_k = -\alpha_k + j\omega_k \quad (9)$$

110 with $\alpha_k > 0$ and $j^2 = -1$. One chooses to index $\lambda_k = -\alpha_k + j\omega_k$ with positive and increasing ω_k contribution from 1 to n and their conjugate from $n + 1$ to $2n$. Hence, $\omega_k > 0$ and $\lambda_{k+n} = \overline{\lambda}_k$, $1 \leq k \leq n$. This said, one can consider the characteristic polynomial $q(\lambda)$ associated to the linear operator in (7) [16, p. 250]:

$$q(\lambda) = \det(\lambda^2 \mathbf{M} + \lambda \mathbf{C} + \mathbf{K}) = \det(\mathbf{M}) \prod_{k=1}^n (\lambda - \lambda_k)(\lambda - \overline{\lambda}_k) \quad (10)$$

115 Finally, the total phase is defined as follows:

$$\phi_{\text{tot}}(\omega) := -\angle(\det \mathbf{M}) - \sum_{k=1}^n \angle((j\omega - \lambda_k)(j\omega - \overline{\lambda}_k)) \quad (11)$$

where $\angle(z)$ denotes the angle of the complex number z lying in $] -\pi, \pi]$. In others words, $\phi_{\text{tot}}(\omega)$ is the “unwrapped” version of $\angle(q(j\omega))$. The next few lines demonstrate that the total phase defined in (11) is one to one and onto from \mathbb{R}^+ onto $] -n\pi, 0]$.

120 First, as \mathbf{M} is assumed to be definite and positive, $\det \mathbf{M} > 0$ and $\angle \det \mathbf{M} = 0$.
Then, the range of each partial factor

$$\phi_{\text{tot},k}(\omega) := -\angle((j\omega - \lambda_k)(j\omega - \bar{\lambda}_k)) \quad (12)$$

can be easily established by rewriting it in the following way

$$\phi_{\text{tot},k}(\omega) = -\angle(|\lambda_k|^2 - \omega^2 + j(2\alpha_k)\omega) \quad (13)$$

This function is well known in the frame of structural dynamics; it is strictly decreasing from $[0, +\infty[$ onto $]-\pi, 0]$. It follows that the sum ϕ_{tot} of these n partial factors $\phi_{\text{tot},k}$ is a strictly decreasing function from $[0, +\infty[$ onto $]-n\pi, 0]$. This implies that to each total phase value $\phi_{\text{tot}}^{(j)} \in]-n\pi, 0]$ one and only one ω value can be associated and subsequently one and only one $\hat{\mathbf{u}}$ value by virtue of Eq. (4). Hence, the ϕ_{tot} variable can be used to parametrize the dynamical problem instead of a classical circular frequency parametrization: varying it continuously from 0 to $-n\pi$ let us compute the frf for the first n modes.

130 Instead of studying the frf by solving the following system

$$\begin{cases} \hat{\mathbf{K}}(\omega)\hat{\mathbf{u}} &= \hat{\mathbf{f}} \\ \omega &= \omega^{(j)} \end{cases} \quad (14)$$

for given $\omega^{(j)}$ values in $[0, +\infty[$, one proposes here to consider

$$\begin{cases} \hat{\mathbf{K}}(\omega)\hat{\mathbf{u}} &= \hat{\mathbf{f}} \\ \phi_{\text{tot}}(\omega) &= \phi_{\text{tot}}^{(j)} \end{cases} \quad (15)$$

for given $\phi_{\text{tot}}^{(j)}$ values in $]-n\pi, 0]$.

This new formulation implies to solve a real nonlinear constraint equation instead of a trivial equation to define ω value. Moreover, the current definition of the total phase requires the evaluation of all the eigenvalues λ_k which can be a costly and inaccurate procedure for large systems: Sec. 3 proposes a preconditioning method and an approximation of $\phi_{\text{tot}}(\omega)$ for low frequencies which requires only the first eigenvalues evaluation. Finally, it is important to notice that, when uncertainties are introduced, the classical formulation (14) let the circular frequency be a non random variable while the constraint equation in system (15) depends on the system random matrices via eigenvalues $\tilde{\lambda}_k$ and hence, ω becomes a random variable:

$$\phi_{\text{tot}}(\tilde{\omega}) = -\angle(\det \tilde{\mathbf{M}}) - \sum_{k=1}^n \angle((j\tilde{\omega} - \tilde{\lambda}_k)(j\tilde{\omega} - \bar{\tilde{\lambda}}_k)) \quad (16)$$

The systems considered in the random case are then:

$$\begin{cases} \tilde{\mathbf{K}}(\omega)\tilde{\mathbf{u}} &= \hat{\mathbf{f}} \\ \omega &= \omega^{(j)} \end{cases} \quad (17)$$

145 for given $\omega^{(j)}$ values in $[0, +\infty[$, and

$$\begin{cases} \tilde{\mathbf{K}}(\tilde{\omega})\tilde{\mathbf{u}} &= \tilde{\mathbf{f}} \\ \tilde{\phi}_{\text{tot}}(\tilde{\omega}) &= \phi_{\text{tot}}^{(j)} \end{cases} \quad (18)$$

for given $\phi_{\text{tot}}^{(j)}$ values in $] -n\pi, 0]$.

2.2. Combination with Polynomial Chaos

150 First, the main points of a Polynomial Chaos expansion are briefly reminded. Then, the combination with the problem considered – Eq. (17) or Eq. (18) – is exposed leading to two different global algorithms.

2.2.1. Polynomial Chaos: main points and notations

155 Only the guidelines of the Polynomial Chaos expansion (PCE) are recalled here. A dimension-one stochastic space is considered: only one random variable ξ is used to introduce randomness in the system. The reader is referred to [19] and references therein for a complete presentation of PCE.

Let $(\Theta, \mathcal{A}, \mathbb{P})$ denote a probability space with Θ the event space, \mathcal{A} the σ -algebra on Θ and \mathbb{P} a probability measure. The probability density function (pdf) associated to a random variable U is denoted p_U . U expected value is defined as:

$$\mu_U = \mathbb{E}[U] = \int_{\Theta} U(\theta) d\mathbb{P}(\theta) = \int_{\mathbb{R}} u p_U(u) du \quad (19)$$

160 and its standard deviation is denoted σ_U :

$$\sigma_U = \sqrt{\mathbb{E}[(U - \mu_U)^2]} \quad (20)$$

With these notations, the random variable ξ is a function from Θ onto \mathbb{R} :

$$\xi : \begin{array}{ccc} \Theta & \longrightarrow & \mathbb{R} \\ \theta & \longmapsto & \xi(\theta). \end{array} \quad (21)$$

Considering a second-order random process X , the Polynomial Chaos expansion proposes to express it as a polynomial series X_p using a set of N_p orthogonal polynomials in the variable ξ and denoted ψ_k :

$$X(\theta) = X_p(\xi(\theta)) := \sum_{n=0}^{N_p-1} x_n \psi_k(\xi(\theta)) \quad (22)$$

165 where the order N_p is theoretically infinite for general situations.

The deterministic coefficients x_n can be evaluated using either an intrusive method or a non-intrusive one. The intrusive method follows a Galerkin approach: Eq. (22) is introduced in the equations governing X and these equations are projected onto the set of orthogonal polynomials ψ_k . The non-intrusive 170 method uses the orthogonality of the polynomials with respect to a inner product denoted $\langle \bullet, \bullet \rangle$:

$$x_n = \frac{\langle X, \psi_k \rangle}{\langle \psi_k, \psi_k \rangle} \quad (23)$$

where the numerator is usually evaluated using a quadrature rule.

The intrusive method provides a set of $n \times N_p$ coupled algebraic equations and often requires a special implementation while the non-intrusive approach determines the set of coefficients x_n one after the other in an independent manner. Already existing codes can then be used to evaluate X realizations needed for the quadrature.

The choice of the polynomial basis is somehow arbitrary; however some bases can be considered as optimal to describe common distributions [3]. In the present case and throughout the paper, it will be assumed that the random variable ξ follows a uniform distribution over $[-1, 1]$:

$$p_\xi(x) = \begin{cases} \frac{1}{2} & \text{if } -1 \leq x \leq 1 \\ 0 & \text{otherwise} \end{cases} \quad (24)$$

This makes the Legendre polynomial basis the most natural choice. The first 6 polynomials (with degree less or equal to 5) are:

$$\begin{aligned} \psi_0(x) &= 1 & \psi_3(x) &= \frac{1}{2}(5x^3 - 3x) \\ \psi_1(x) &= x & \psi_4(x) &= \frac{1}{8}(35x^4 - 30x^2 + 3) \\ \psi_2(x) &= \frac{1}{2}(3x^2 - 1) & \psi_5(x) &= \frac{1}{8}(63x^5 - 70x^3 + 15x) \end{aligned} \quad (25)$$

This set of polynomials is orthogonal with respect to the following inner product

$$\langle f, g \rangle = \frac{1}{2} \int_{-1}^1 f(x)g(x)dx \quad (26)$$

and hence,

$$\langle X, \psi_k \rangle = E[X \psi_k] \quad (27)$$

In the Illustrations section (Sec. 4), PCE coefficients x_n will be evaluated following a non-intrusive approach by using a Gauss-Legendre quadrature rule to compute Eq. (23) numerator.

Once PCE coefficients x_n are evaluated, there are two ways to post-process the result. First, the mean and variance can be directly computed (provided $\psi_0(x) = 1$):

$$E[X_p] = x_0 \langle \psi_0, \psi_0 \rangle \quad \text{and} \quad E[(X_p - E[X_p])^2] = \sum_{n=1}^{N_p-1} x_n^2 \langle \psi_k, \psi_k \rangle \quad (28)$$

Second, the cumulative distribution function (cdf) and the pdf can be evaluated based on MC simulations. The difference with the usual processing is that X realizations are computed using its PCE X_p (i.e. Eq. (22)) rather than solving the direct problem. This saves a lot of computational time and resource when the samples are large.

2.2.2. Global algorithms

200 In this paper, a non-intrusive method is used to evaluate PCE coefficients: a Gauss-Legendre quadrature with N_{GL} nodes is used to evaluate the inner product Eq. (26) involved in Eq. (23). Depending on the method applied – constant frequency or constant total phase – the quantities whose PCE has to be evaluated differ.

205 In the classical case (Eq. (17)), for N frequency values $\omega^{(j)}$ of interest, the PCE of $\tilde{\mathbf{u}}$ has to be evaluated: the linear system (17) has to be solved N_{GL} times for a dynamic stiffness matrix evaluated at the quadrature nodes $\xi_{GL}^{(i)}$, $1 \leq i \leq N_{GL}$. Algorithm 1 depicts the global procedure. $\hat{\mathbf{u}}_{\omega}^{(j,i)}$ denotes the realization of $\tilde{\mathbf{u}}$ for $\omega^{(j)}$ and $\xi_{GL}^{(i)}$ while $\tilde{\mathbf{u}}_{\omega}^{(j)}$ denotes the random vector solution of Eq. (17) for $\omega^{(j)}$.
210

Algorithm 1: Global procedure considering a constant frequency

Data: System random matrices, Gauss-Legendre quadrature nodes $\xi_{GL}^{(i)}$ and $\omega^{(j)}$ discrete values of interest.

- 1 **foreach** $\omega^{(j)}$, $1 \leq j \leq N$ **do**
- 2 **foreach** $\xi_{GL}^{(i)}$, $1 \leq i \leq N_{GL}$ **do**
- 3 | Compute $\hat{\mathbf{u}}_{\omega}^{(j,i)}$ solution of Eq. (17).
- 4 **end**
- 5 | Compute $\tilde{\mathbf{u}}_{\omega}^{(j)}$ PCE using quadrature rule (23).
- 6 **end**

The procedure using a constant total phase is depicted in Algorithm 2. In this case, given values are those of total phase: $\phi_{tot}^{(j)}$, $1 \leq j \leq N$. For each of these values, one has to compute the PCE of both $\tilde{\mathbf{u}}$ and $\tilde{\omega}$, solutions of Eq. (18). As the computation of $\tilde{\phi}_{tot}$ implies the computation of $\{\tilde{\mathbf{M}}, \tilde{\mathbf{C}}, \tilde{\mathbf{K}}\}$ eigenvalues, it is obviously more interesting to switch **foreach** instructions of the previous algorithm. $\hat{\mathbf{u}}_{\phi}^{(j,i)}$ (resp. $\omega_{\phi}^{(j,i)}$) denotes the realization of $\tilde{\mathbf{u}}$ (resp. $\tilde{\omega}_{\phi}$) for $\phi_{tot}^{(j)}$ and $\xi_{GL}^{(i)}$ while $\tilde{\mathbf{u}}_{\phi}^{(j)}$ (resp. $\tilde{\omega}_{\phi}^{(j)}$) denotes the random vector (resp. 215

random variable) solution of Eq. (18) for $\phi_{\text{tot}}^{(j)}$.

Algorithm 2: Global procedure considering a constant total phase

Data: System random matrices, Gauss-Legendre quadrature nodes $\xi^{(k)}$ and $\phi_{\text{tot}}^{(j)}$ discrete values of interest.

220 **1** **foreach** $\xi_{GL}^{(i)}$, $1 \leq i \leq N_{GL}$ **do**
2 Compute eigenvalues λ_k solutions of $\det(\lambda_k^2 \tilde{\mathbf{M}} + \lambda_k \tilde{\mathbf{C}} + \tilde{\mathbf{K}}) = 0$.
3 **foreach** $\phi_{\text{tot}}^{(j)}$, $1 \leq j \leq N$ **do**
4 Compute $\omega_{\phi}^{(j,i)}$ and $\hat{\mathbf{u}}_{\phi}^{(j,i)}$ solution of Eq. (18).
5 **end**
6 **end**
7 **foreach** $\phi_{\text{tot}}^{(j)}$, $1 \leq j \leq N$ **do**
8 Compute $\tilde{\mathbf{u}}_{\phi}^{(j)}$ and $\tilde{\omega}_{\phi}^{(j)}$ PCE using quadrature rule (23).
9 **end**

2.3. Going back to a constant frequency description from a constant total phase study

225 A last point which will be illustrated in Sec. 4 is the possibility to rebuild a constant frequency view of the stochastic response when doing the primary calculations using a constant total phase approach described in Eq. (18). Basically, it relies on a linear interpolation of the results obtained for discrete total phase values $\phi_{\text{tot}}^{(j)}$ in order to evaluate $\tilde{\mathbf{u}}(\omega_t, \xi^{(i)})$ for each $\xi^{(i)}$ of the sample where ω_t denotes the target frequency. First, one looks for the total phase discrete values which embrace ω_t for the given $\xi^{(i)}$ value:

$$\text{find } j_0 \in \{1, \dots, N\} \text{ such that } \omega_{\phi}^{(j_0, i)} \leq \omega_t \leq \omega_{\phi}^{(j_0+1, i)} \quad (29)$$

230 then, $\theta \in [0; 1]$ is defined such that

$$\omega_t = (1 - \theta)\omega_{\phi}^{(j_0, i)} + \theta\omega_{\phi}^{(j_0+1, i)} \quad (30)$$

and finally $\tilde{\mathbf{u}}$ is evaluated using the following interpolation:

$$\tilde{\mathbf{u}}(\omega_t, \xi^{(i)}) = (1 - \theta)\hat{\mathbf{u}}_{\phi}^{(j_0, i)} + \theta\hat{\mathbf{u}}_{\phi}^{(j_0+1, i)} \quad (31)$$

Algorithm 3 states the different steps to get $\tilde{\mathbf{u}}_t^{(i)} = \tilde{\mathbf{u}}(\omega_t, \xi^{(i)})$ values.

Algorithm 3: Evaluating constant frequency stochastic response from a constant total phase study

Data: $\tilde{\mathbf{u}}_\phi^{(j)}$ and $\tilde{\omega}_\phi^{(j)}$ PCE for $\phi_{\text{tot}}^{(j)}$ discrete values, $1 \leq j \leq N$; $\xi^{(i)}$, sample of random variable values, $1 \leq i \leq N_s$; ω_t frequency of interest.

- 1 **foreach** $\xi^{(i)}$, $1 \leq i \leq N_s$ **do**
 - 2 Compute $\tilde{\omega}_\phi^{(j,i)} = \tilde{\omega}_\phi^{(j)}(\xi^{(i)})$, $1 \leq j \leq N$ using $\tilde{\omega}_\phi^{(j)}$ PCE.
 - 3 Find j_0 such that $\tilde{\omega}_\phi^{(j_0,i)} \leq \omega_t \leq \tilde{\omega}_\phi^{(j_0+1,i)}$.
 - 4 Compute $\theta = (\omega_t - \tilde{\omega}_\phi^{(j_0,i)}) / (\tilde{\omega}_\phi^{(j_0+1,i)} - \tilde{\omega}_\phi^{(j_0,i)})$.
 - 5 Compute $\tilde{\mathbf{u}}_\phi^{(j_0,i)} = \tilde{\mathbf{u}}_\phi^{(j_0)}(\xi^{(i)})$ using $\tilde{\mathbf{u}}_\phi^{(j)}$ PCE.
 - 6 Compute $\tilde{\mathbf{u}}_\phi^{(j_0+1,i)} = \tilde{\mathbf{u}}_\phi^{(j_0+1)}(\xi^{(i)})$ using $\tilde{\mathbf{u}}_\phi^{(j)}$ PCE.
 - 7 Compute $\tilde{\mathbf{u}}_t^{(i)} = \tilde{\mathbf{u}}(\omega_t, \xi^{(i)})$ using Eq. (31).
 - 8 **end**
 - 9 Process $\tilde{\mathbf{u}}_t^{(i)}$, $1 \leq i \leq N_s$ sample.
-

3. Computational considerations

235 First, as complex numbers angles are defined modulo 2π , it is obvious that the total phase should not be computed using the angle of the product of the n factors $(j\omega - \lambda_k)(j\omega - \bar{\lambda}_k)$ but as the sum of the angle of each factor, that is the sum of each $\phi_{\text{tot},k}$ defined in Eq. (12). This said, this section addresses first the choice of a linearisation used to process the QEP and then the expression of an approximation which requires only the smallest eigenvalues. The last subsection is devoted to the efficiency and accuracy of this approximation.

240

3.1. Choice of a linearisation

Most methods used to compute the eigenvalues solution of Eq. (10) rely on a linearisation of the QEP (7) [16, Sec. 5]. Different linearisations are available in the literature [20], [16, Sec. 3.4], [21, Sec. 9.3]. The usual formulation is as follows:

245

$$\underbrace{\begin{bmatrix} \mathbf{U} & \mathbf{0} \\ \mathbf{0} & \mathbf{M} \end{bmatrix}}_B \dot{\mathbf{x}} + \underbrace{\begin{bmatrix} \mathbf{0} & -\mathbf{U} \\ \mathbf{K} & \mathbf{C} \end{bmatrix}}_A \mathbf{x} = \begin{Bmatrix} \mathbf{0} \\ \mathbf{f} \end{Bmatrix} \quad (32)$$

where \mathbf{U} has to be invertible so as to ensure that $x_{k+n} = dx_k/dt$, $1 \leq k \leq n$. The choice of \mathbf{U} depends on the properties of system matrices [22].

The one linearisation used here is the energy phase space linearisation proposed by Veselić [17, Sec. 3.2]: let \mathbf{L}_K and \mathbf{L}_M be such that

250

$$\mathbf{K} = \mathbf{L}_K \mathbf{L}_K^T \text{ and } \mathbf{M} = \mathbf{L}_M \mathbf{L}_M^T \quad (33)$$

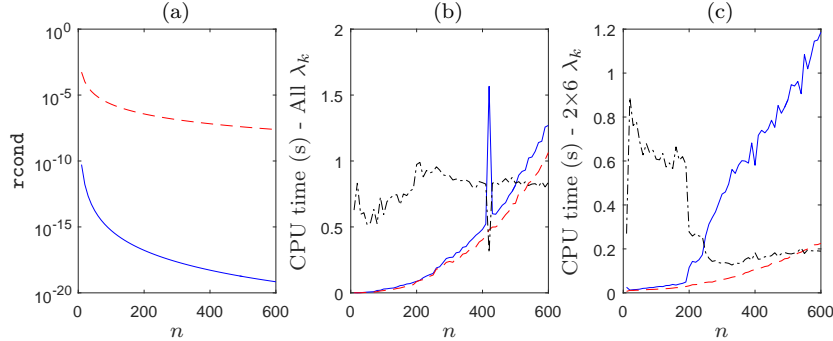


Figure 1: Reciprocal condition number (a) and CPU time to solve the full eigenvalue problem using `eig` (b) or to compute only the first 2×6 smallest eigenvalues using `eigs(•, 'sm', 12)` (c) depending on the system size n and the linearisation. Solid (blue) line: classical linearisation; Dashed (red) line: energy phase space linearisation; Dashed dotted (black) line: ratio between energy phase space and classical linearisation.

in what follows the Cholesky decomposition is used to compute L_{\bullet} matrices. Then, use the following change of variables

$$\mathbf{u} = \mathbf{L}_K^{-T} \mathbf{x}_1, \dot{\mathbf{u}} = \mathbf{L}_M^{-T} \mathbf{x}_2 \quad (34)$$

to rewrite the dynamical equation (1):

$$\mathbf{M} \mathbf{L}_M^{-T} \dot{\mathbf{x}}_2 + \mathbf{C} \mathbf{L}_M^{-T} \mathbf{x}_2 + \mathbf{K} \mathbf{L}_K^{-T} \mathbf{x}_1 = \mathbf{f}(t) \quad (35a)$$

$$\mathbf{L}_M^{-T} \mathbf{x}_2 = \mathbf{L}_K^{-T} \dot{\mathbf{x}}_1 \quad (35b)$$

After pre-multiplying Eq. (35a) by \mathbf{L}_M^{-1} and a few transformations, one gets an equivalent linear system with size $2n$:

$$\dot{\mathbf{x}} = \underbrace{\begin{bmatrix} \mathbf{0} & \mathbf{L}_K^T \mathbf{L}_M^{-T} \\ -\mathbf{L}_M^{-1} \mathbf{L}_K & -\mathbf{L}_M^{-1} \mathbf{C} \mathbf{L}_M^{-T} \end{bmatrix}}_{\mathbf{A}_e} \mathbf{x} + \begin{Bmatrix} \mathbf{0} \\ \mathbf{L}_M^{-1} \mathbf{f} \end{Bmatrix}, \mathbf{x} = \begin{Bmatrix} \mathbf{x}_1 \\ \mathbf{x}_2 \end{Bmatrix} \quad (36)$$

255 Linear problems (1), (32) and (36) have the same eigenvalues [17, Sec. 14] but
not the same numerical properties as emphasized in Fig. 1. A simple clamped-
free bending beam finite element model with a varying number of dofs is gener-
ated; modal damping is introduced once mass and stiffness matrices are assem-
sembled. The characteristics of the beam are the same than the clamped beam
260 example studied in Sec. 4.2 except for limit conditions which are a perfect clamp-
ing on one end and with the other end being perfectly free; hence this model
is fully deterministic. For each system size, linearisation (32) with $\mathbf{U} = -\mathbf{K}$
and (36) are compared using first, the reciprocal condition number of $\mathbf{B}^{-1} \mathbf{A}$
(resp. \mathbf{A}_e) evaluated via Matlab function `rcond`, then the CPU times for comput-
265 ing all the eigenvalues using Matlab command `eig(-B\A)` (resp. `eig(Ae)`)
or to compute the first 12 smallest eigenvalues – that is the first 6 λ_k and their

conjugates $\overline{\lambda_k}$ – using `eigs(-B\A, 'sm', 12)` (resp. `eigs(Ae, 'sm', 12)`). CPU times include \mathbf{A} and \mathbf{B} matrices creation (resp. \mathbf{A}_e as well as \mathbf{L}_M and \mathbf{L}_K evaluation); displayed CPU times are the means over 5 identical computations for each case.

First, the reciprocal condition number is higher when using the energy phase space linearisation. Second, energy phase space linearisation leads to smaller CPU times when one evaluates the eigenvalues, especially when only the first smallest eigenvalues are to be extracted which is interesting considering the total phase approximation detailed below.

Similar results are obtained when using $\mathbf{U} = \mathbf{M}$.

3.2. Total phase approximation

In order to avoid the computation of all the eigenvalues λ_k , one can first, use a truncation to eigenvalues matching the range of interest, that is, low frequencies: only N_λ eigenvalues are kept, using the following criterion:

$$|\omega_k| \leq 2\pi f_{\max} r \quad (37)$$

where f_{\max} denotes the maximum frequency of interest and r a security coefficient greater than 1. Doing so, one also decreases the number of factors $\phi_{\text{tot},k}(\omega)$ involved in the summation (11) which leads to a faster evaluation and an easier resolution of the constraint equation.

The second step is, as when dealing with model reduction, to use a “static compensation” to take higher order modes influence into account. Considering small circular frequency values ω compared to eigen circular frequencies ω_k for $k > N_\lambda$, one can write, for each partial factor

$$\phi_{\text{tot},k}(\omega) = -\frac{2\alpha_k}{|\lambda_k|^2}\omega + o(\omega^2) \quad (38)$$

Hence, an approximation of ϕ_{tot} using a linear correction can be written:

$$\phi_{\text{tot}}(\omega) \approx -\sum_{k=1}^{N_\lambda} \angle((j\omega - \lambda_k)(j\omega - \overline{\lambda_k})) + \left(\sum_{k=N_\lambda+1}^n -\frac{2\alpha_k}{|\lambda_k|^2} \right) \omega \quad (39)$$

This approximation still requires the evaluation of higher order eigenvalues λ_k . To avoid their computation one uses one of the following equalities which are demonstrated in [Appendix B](#), depending on the linearisation used (Eq. (32) or Eq. (36)):

$$\sum_{k=1}^n -\frac{2\alpha_k}{|\lambda_k|^2} = -\text{tr}(\mathbf{K}^{-1}\mathbf{C}) = -\text{tr}(\mathbf{L}_K^{-1}\mathbf{C}\mathbf{L}_K^{-T}) \quad (40)$$

This finally leads to an approximation of the total phase which requires the evaluation of $\mathbf{K}^{-1}\mathbf{C}$ or $\mathbf{L}_K^{-1}\mathbf{C}\mathbf{L}_K^{-T}$ and the first N_λ eigenvalues λ_k only; this

final expression is denoted ϕ_{N_λ} :

$$\phi_{N_\lambda}(\omega) = -\sum_{k=1}^{N_\lambda} \angle((j\omega - \lambda_k)(j\omega - \bar{\lambda}_k)) + \left(-\text{tr}(\mathbf{L}_K^{-1} \mathbf{C} \mathbf{L}_K^{-T}) - \sum_{k=1}^{N_\lambda} -\frac{2\alpha_k}{|\lambda_k|^2} \right) \omega \quad (41)$$

The previous expression is written in the case of an energy phase space linearisation: this is the only one used in the rest of the paper.

3.3. Efficiency and accuracy results

The numerical efficiency and accuracy of the several ways to evaluate the total phase are tested using the same clamped-free beam model as in Sec. 3.1. Uncertainty is added in a very simple way:

$$\tilde{\mathbf{K}}(\xi) = \mathbf{K}(1 + 0.05\xi) \quad (42)$$

First, the complexity of several algorithms is examined. On the one hand, all the eigenvalues are evaluated using either linearisation (32) with $\mathbf{U} = -\mathbf{K}$ or the energy phase space linearisation (36). Matlab functions used are `eig(A, -B)` and `eig(Ae)` respectively. On the other hand, following the definition of the approximated total phase (41) with $N_\lambda = 6$, only the first 12 smallest eigenvalues λ_k and $\bar{\lambda}_k$, $1 \leq k \leq N_\lambda = 6$ are evaluated using `eigs(Ae, 12, 'sm')` together with the matrix $\mathbf{L}_K^{-1} \mathbf{C} \mathbf{L}_K^{-T}$ whose trace is required. These evaluations are realized for $n \in \{10, 20, \dots, 100, 200, \dots, 1000\}$ and five ξ values each time, $\xi \in \{-1, -0.5, 0, 0.5, 1\}$.

Results are depicted in Fig. 2. Dashed lines match the fitted linear interpolation in log-log scales for each case. First, as expected from results of Sec. 3.1, using an energy phase space linearisation is always cheaper than using a classical linearisation. Second, direct evaluation of all eigenvalues is cheaper for small systems (here, with less than $n = 100$ dofs), while for large systems, computing only some of them becomes a lot cheaper as the difference between the two slopes (3.44 in the first case and 2.01 in the second one) points out even though $\mathbf{L}_K^{-1} \mathbf{C} \mathbf{L}_K^{-T}$ has to be evaluated.

The accuracy of the approximation is now tested: considering the clamped-free beam system for $n = 300$ and the nominal system only ($\xi = 0$), the total phase is evaluated at 10 000 points equally spaced over $[0, 1.1 \times \omega_6]$ using either initial definition (11) or approximation (41) with $N_\lambda = 6$. Both curves are displayed in Fig. 3 along with the relative error generated by the approximation (right-side ordinate axis, dashed dotted line). It appears that the relative error remains very small (less than 0.05%) over the whole frequency range. This example hence seems to indicate that using approximated total phase expression for low frequencies is very reasonable considering the accuracy criterion.

A final test considers the time used for solving the constraint equation in system (15): when the total phase is evaluated using the approximated formulation, less factors are involved and one can expect that it is easier to solve.

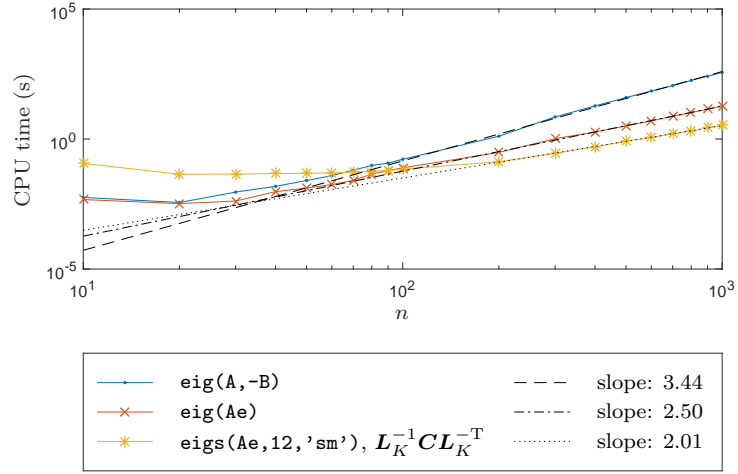


Figure 2: Total phase: complexity with respect to system size n for several computational methods

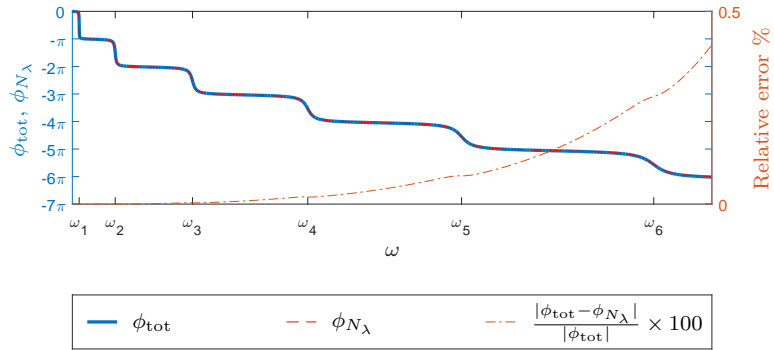


Figure 3: Total phase: accuracy of approximation ϕ_{N_λ} ($N_\lambda = 6$)

To test this hypothesis, the total phase range $[-6\pi, 0]$ is divided in 6 000 points
 330 linearly spaced $\phi_{\text{tot}}^{(j)}$. The constraint equation is then solved for each point in
 decreasing order using `fzero` Matlab function and the previous solution value
 as the initial guess for the current resolution (first guess to initialize the loop
 when $j = 1$ is $\omega = 0$). CPU time is collected once this resolution loop is applied
 10 times successively. When using the initial definition of total phase (11), the
 335 whole procedure costs 55.7 s; when using the approximated expression (41), it
 lasts only 37.8 s, that is 32% less.

Comparison of the cost of global procedures including Polynomial Chaos
 expansions when considering either Eq. (17) or Eq. (18) and using initial to-
 tal phase (11) or approximated total phase (41) expressions will be addressed
 340 through the numerical examples developed in Sec. 4.

4. Illustrations

The proposed method is applied to two systems. The first one is a very
 simple 2 mass-spring damped system which will illustrate the ability of the
 proposed method to return the expected accurate results. The second one is a
 345 beam with imperfect clamping conditions at both ends; it will illustrate the the
 accuracy of the truncated expression for the total phase and the relative cost of
 the methods.

For both systems, the usual approach, using a constant frequency and the
 proposed approach, using a constant total phase will be compared. For the sake
 350 of brevity the two approaches will be further referred to as CFA for Constant
 Frequency Approach and CTPA for Constant Total Phase Approach.

For both examples and both approaches, only one random variable is intro-
 duced and degree 5 Polynomial Chaos with Legendre polynomials expressed in
 Eq. (25) is used. Coefficients are evaluated using a Gauss-Legendre quadrature
 355 rule with 11 nodes for numerator and denominator expressed in Eq. (23). When
 considering CTPA, an energy phase space linearisation is used to solve the QEP.

Stochastic dimension is kept small on purpose so as not to mix the “curse of
 dimensionality” related to polynomial chaos when multiple variables are intro-
 duced in the model and the point of the paper which is a new parametrization
 360 of the dynamical system response in order to get more accurate PCE results.

4.1. 2-dofs system

The first system used to illustrate and compare both approaches is a simple
 2-dofs system depicted in Fig. 4 whose matrices are:

$$\mathbf{M} = \begin{bmatrix} m & 0 \\ 0 & m \end{bmatrix}, \mathbf{C} = \begin{bmatrix} c_1 + c_2 & -c_2 \\ -c_2 & c_2 \end{bmatrix}, \mathbf{K} = \begin{bmatrix} k_1 + k_2 & -k_2 \\ -k_2 & k_2 \end{bmatrix} \quad (43)$$

Only the second mass undergoes an external load: $\mathbf{f}(t) = \{0, 1\}^T \cos(\omega t)$.
 365 Numerical values for nominal system are $m_1 = 1$ kg, $c_1 = 1$ kg.s⁻¹, $c_2 =$

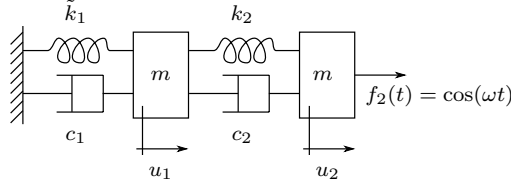


Figure 4: 2-dofs system with random stiffness \tilde{k}_1

$0.2 \text{ kg}\cdot\text{s}^{-1}$, $k_1 = 100 \text{ N}\cdot\text{m}^{-1}$ and $k_2 = 200 \text{ N}\cdot\text{m}^{-1}$.

In the random case, the first spring stiffness depends on a random variable ξ :

$$\tilde{k}_1 = k_1(1 + \xi\Delta k_1) \quad (44)$$

with $\Delta k_1 = 0.75$; ξ is assumed to have a uniform distribution over $[-1, 1]$.

A complex formulation is used to solve the linear dynamical problem: unknowns are the complex variables \hat{u}_1 and \hat{u}_2 .

A similar case with a Gaussian random variable instead of a uniform one is illustrated in [Appendix D](#).

4.1.1. MCS results

First, Monte Carlo simulations are run in order to visualize the differences between the two approaches. The dynamical system is solved for 100 001 values of ξ equally spaced over $[-1, 1]$ and for 201 values of $\omega = 2\pi f$ equally spaced over $[0, 5] \times 2\pi$ to illustrate the CFA and for 201 values of ϕ_{tot} over $[-1.9318 \times \pi, 0]$ which are not equally spaced (see [Appendix C](#)) to illustrate the CTPA. These simulations will serve as references to evaluate the accuracy of each approach.

Fig. 5 shows the complex response of the second dof (\hat{u}_2) for different values of ξ : amplitude $|\hat{u}_2|$ and angle $\angle \hat{u}_2$ (that is the phase between u_2 and the excitation) are plotted versus the excitation frequency f and the total phase ϕ_{tot} is superimposed to the angle in the lower plots. This shows first that contrarily to the angle, the total phase is continuously decreasing when the frequency increases and that important total phase slopes happen around resonances and with values centred around $-\pi/2$ and $-3\pi/2$.

Second, two frequencies are shown on the plots (1.05 Hz and 3.4 Hz). Considering different values of ξ , it is obvious that for a given frequency, very different responses happen in terms of amplitude, angle, and total phase. On the contrary, considering the response for a given total phase value (-0.5π or -1.5π for instance) narrows the variability of the responses. This latter observation is even more obvious when looking at Fig. 6. Amplitude and angle values are rendered via a grey scale and visualized in either a (f, ξ) plane in column (a) or in (ϕ_{tot}, ξ) plane in column (b). For both views, the paths of a constant frequency study and a constant total phase study are displayed: constant total phase paths do not cross very different grey tones that is, tend to describe similar states of the system in terms of amplitude and angle, whereas constant

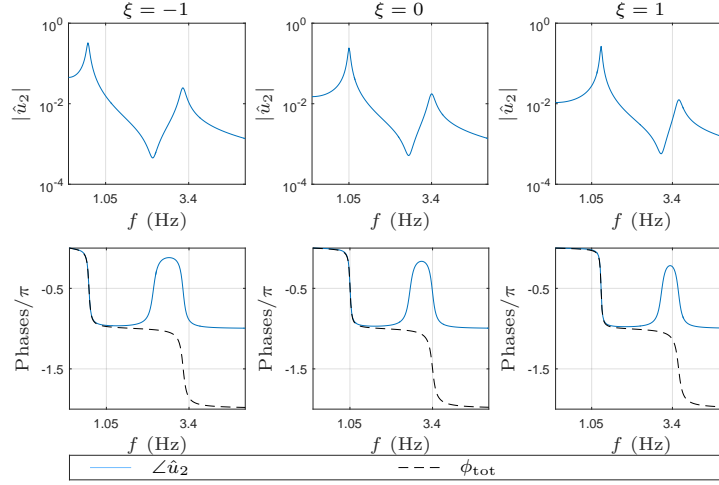


Figure 5: 2-dofs, MCS – System second dof response (\hat{u}_2) for different ξ values. Vertical grid lines denote the two frequencies used for further constant frequency study while the horizontal grid lines in the phases plots denotes the two total phase values used for further constant total phase study.

frequency paths embrace large ranges of grey tones which implies larger variations to be rendered via PCE. Similar results could be plotted for the first dof \hat{u}_1 .

4.1.2. PCE results

Only the amplitudes $|\hat{u}_k|$ (not angles) are fitted using polynomial chaos. Both algorithms (Algorithm 1 for CFA and Algorithm 2 for CTPA) are applied using the same samples in ω or ϕ_{tot} as for MCS. For CTPA, total phase formula used is Eq. (11) without truncation as the system is small and all its modes are within the frequency range of interest. Fig. 7, 8 and 9 compare results obtained via both methods with MCS results to evaluate their global accuracy. The upper row in Fig. 7 shows the values of $|\hat{u}_2|$ evaluated from PCE for each of the 201 $\omega^{(j)}$ values (column (a)) or $\phi_{\text{tot}}^{(j)}$ values (column (b)). The lower row shows the relative error between PCE and MCS. The error scales for both methods are very different: more than 100% error arise with the CFA while errors are less than 5% in the case of CTPA. This shows that CTPA is accurate even for low PCE orders. Fig. 8 provides more general indicators, namely error on mean and standard deviation for each method. It shows that CFA errors in mean and variance increase especially around resonances while the errors stay contained in the CTPA case. As ω becomes a random variable in the CTPA case, the same error plots are provided in Fig. 9 to show that the nonlinear constraint equation of system (18) is solved with a great accuracy too.

Fig. 10 compare MCS and PCE results for CFA at the eigenfrequencies of the nominal system: $|\hat{u}_k|$ dependencies to ξ are very poorly represented and the

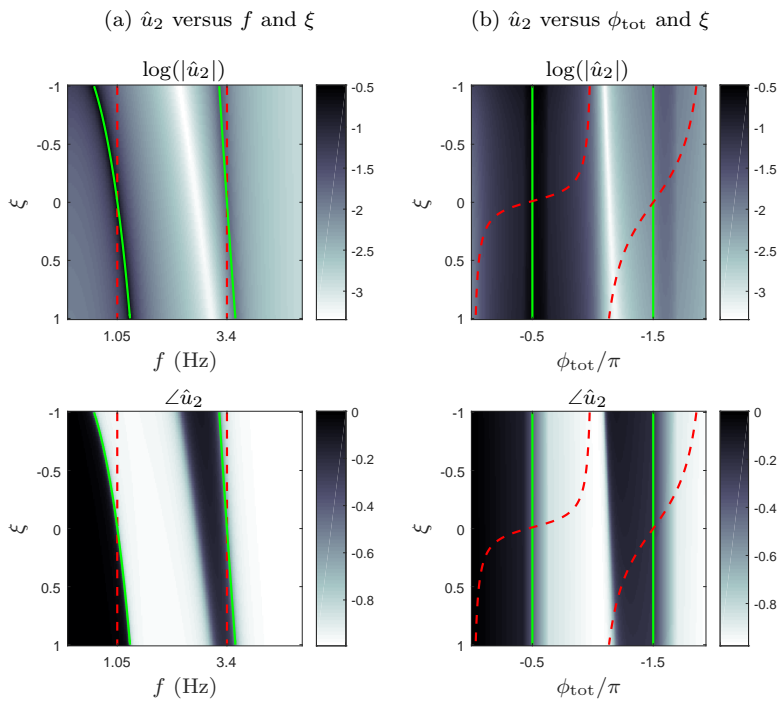


Figure 6: 2-dofs, MCS – System second dof response (\hat{u}_2) versus (a) f and ξ , (b) ϕ_{tot} and ξ . Dashed (red) lines: constant frequency paths; Solid (green) lines: constant total phase paths.

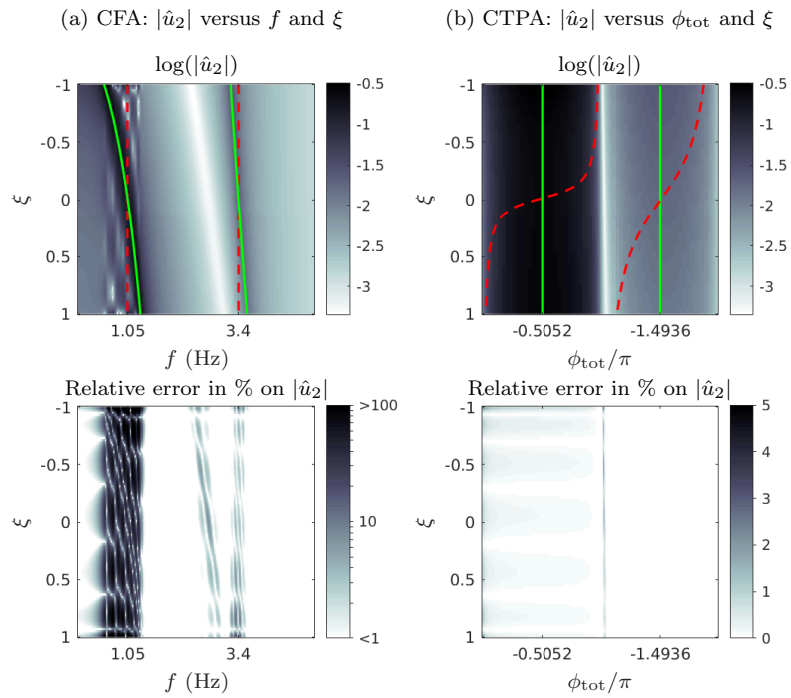


Figure 7: 2-dofs, PCE, Accuracy comparison – System second dof response amplitude ($|\hat{u}_2|$) and error on response amplitude compared to MCS results. (a) PCE results using a CFA, (b) PCE results using a CTPA.

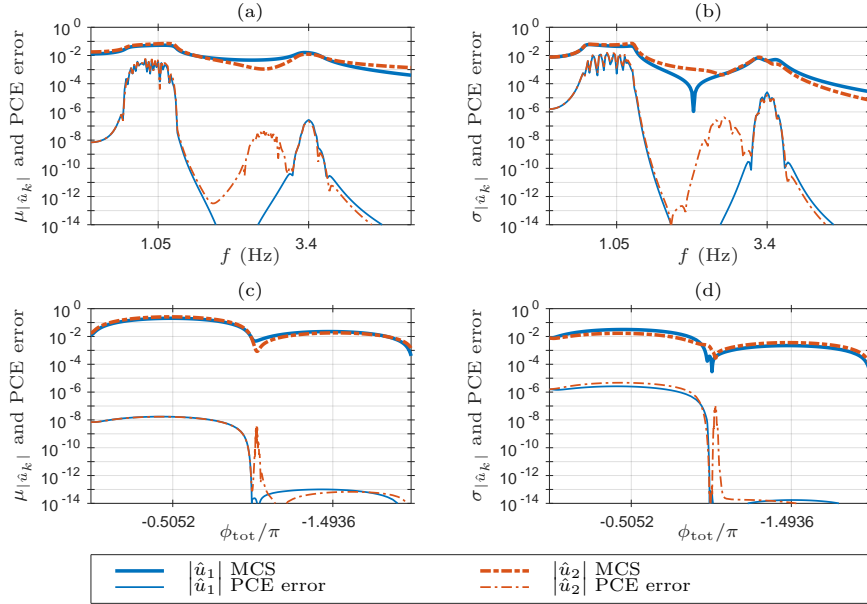


Figure 8: 2-dofs, PCE, Accuracy comparison – Comparison of MCS and PCE results using global indicators over the full frequency range when using (a,b) CFA and (c,d) CTPA. (a,c) mean and (b,d) standard deviation of $|\hat{u}_k|$; thick lines depict MCS results while thin lines denote the absolute difference between MCS and PCE results.

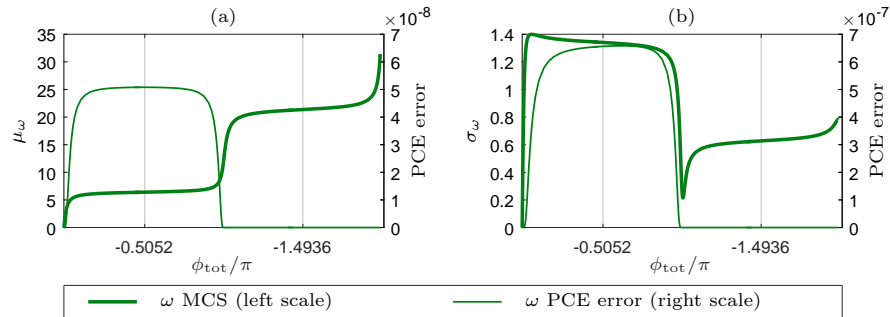


Figure 9: 2-dofs, PCE, Accuracy comparison – Comparison of MCS and PCE results using global indicators over the full frequency range when using CTPA. (a) mean and (b) standard deviation of ω ; thick lines depict MCS results (values are to be read on left scale) while thin lines denote the absolute difference between MCS and PCE results (values are to be read on right scales).

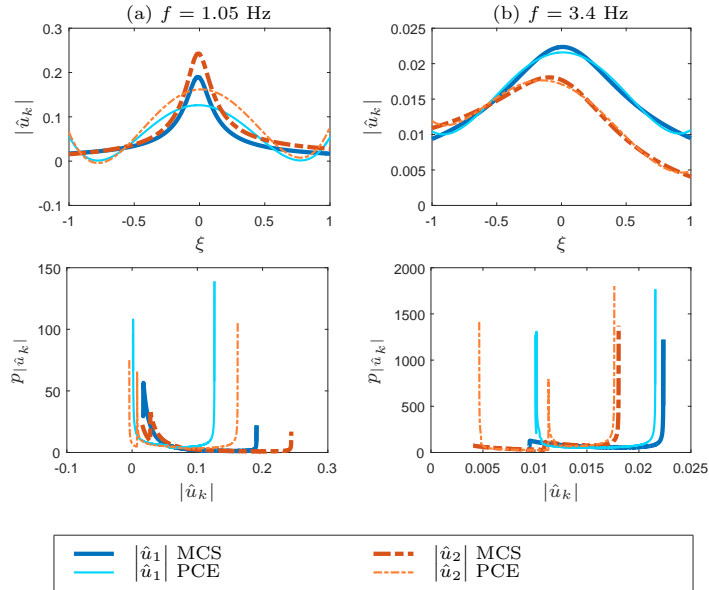


Figure 10: 2-dofs, CFA – Comparison of MCS and PCE results for constant frequencies. Upper plots: $|\hat{u}_k|$ versus ξ ; lower plots: pdf of $|\hat{u}_k|$.

resulting pdfs do not match the expected ones at all. On the contrary, in case of a CTPA, $|\hat{u}_k|$ polynomial representation match the real dependencies very accurately leading to very accurate pdfs as depicted in Fig. 11.

Finally, Algorithm 3 is applied to evaluate $|\hat{u}_k|$ distributions for eigenfrequencies from CTPA results. Fig. 12 shows that it leads to much more accurate results than when using CFA directly (Fig. 10).

The case when a Gaussian random variable is used illustrated in Appendix D demonstrates that the accuracy does not depend on the law that the random variable follows: the same qualitative results are found.

4.2. Clamped beam

The second application is a bending beam with imperfect clamping conditions at both ends; this can arise for example when assemblies with bolted joints are studied. The system is depicted in Fig. 13. It consists in a beam with length $L = 1$ m, width $b = 1$ cm and height $h = 2$ cm made of steel (Young modulus $E = 2 \cdot 10^{11}$ Pa, density $\rho = 7800$ kg.m⁻³). A finite element model with 100 nodes and 2 dofs per node is computed leading to mass and stiffness matrices, \mathbf{M} and \mathbf{K}_b respectively. One translational and one rotational spring (with respective stiffness k_t and k_r) link each extremity to the ground; these stiffness are assumed to introduce uncertainty modelled as follows: $\tilde{k}_t = 10^7(1 + 0.5\xi)$ N.m⁻¹ and $\tilde{k}_r = 10^5(1 + 0.8\xi)$ N.m.rad⁻¹ where ξ follows a uniform law over $[-1, 1]$. This leads to random translational and rotational stiffness matrices $\tilde{\mathbf{K}}_t(\xi)$ and

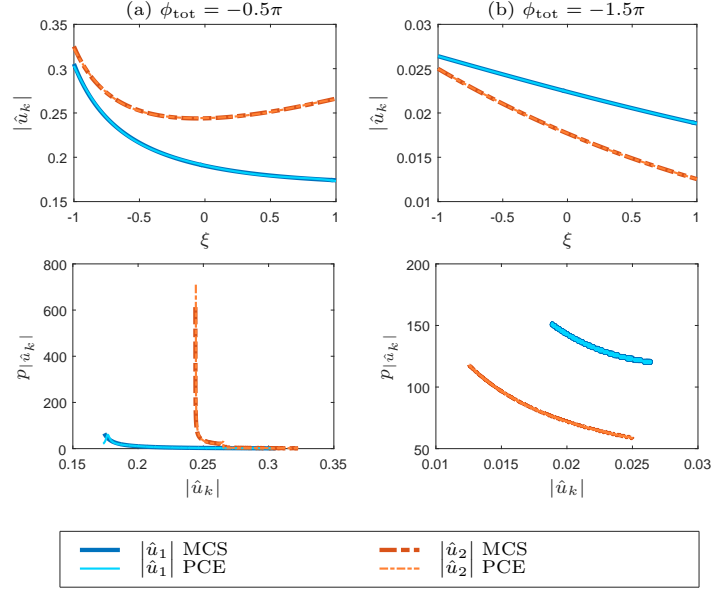


Figure 11: 2-dofs, CTPA – Comparison of MCS and PCE results for constant total phases. Upper plots: $|\hat{u}_k|$ versus ξ ; lower plots: pdf of $|\hat{u}_k|$.

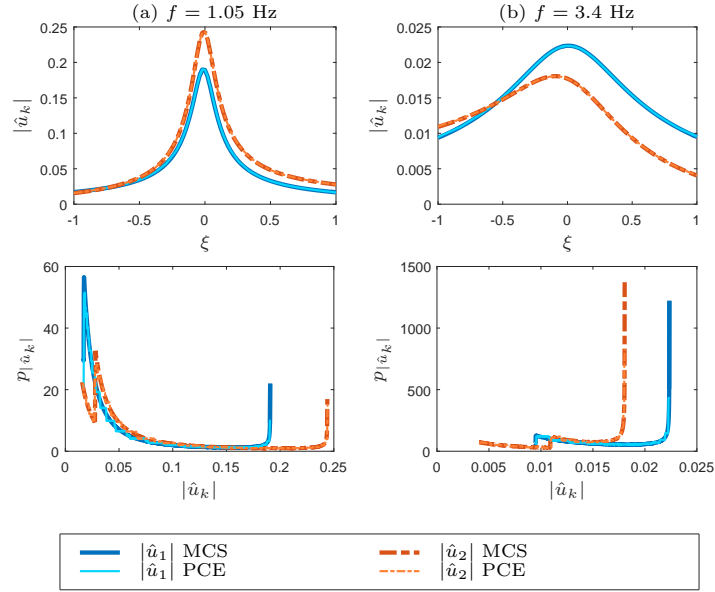


Figure 12: 2-dofs, Constant frequency results rebuilt from CTPA results – Comparison of MCS and PCE results for constant frequencies. Upper plots: $|\hat{u}_k|$ versus ξ ; lower plots: pdf of $|\hat{u}_k|$.

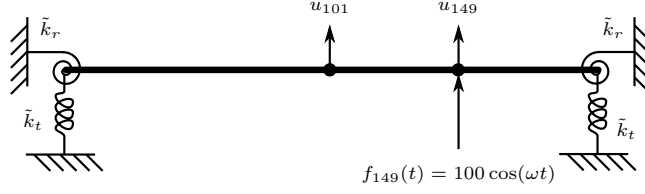


Figure 13: Clamped beam with random stiffness \tilde{k}_t and \tilde{k}_r .

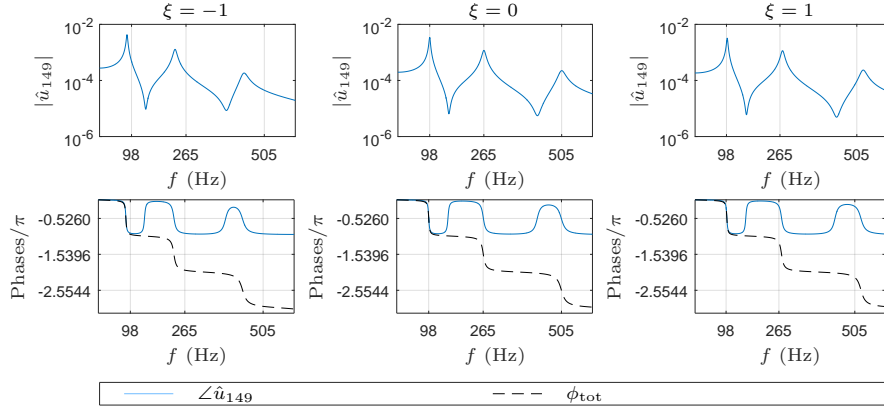


Figure 14: Beam, MCS – System 149-th dof response (\hat{u}_{149}) for different ξ values. Vertical grid lines denote the three frequencies used for further constant frequency study while the horizontal grid lines in the phases plots denotes the three total phase values used for further constant total phase study.

$\tilde{\mathbf{K}}_r(\xi)$ which are added to \mathbf{K}_b to get the system random stiffness matrix:

$$\tilde{\mathbf{K}}(\xi) = \mathbf{K}_b + \tilde{\mathbf{K}}_t(\xi) + \tilde{\mathbf{K}}_r(\xi) \quad (45)$$

To ensure sub-critical damping for all the modes, modal damping is applied. First, undamped modes are evaluated using mass matrix \mathbf{M} and nominal system stiffness matrix $\tilde{\mathbf{K}}(\xi = 0)$. This provides 200 circular eigenfrequencies ω_k and eigenvectors φ_k . Then the diagonal damping matrix in the modal basis is created $\tilde{\mathbf{C}} = \text{diag}(2\eta_k\omega_k)$ with damping rates η_k logarithmically spaced between $\eta_1 = 0.02$ and $\eta_{200} = 0.2$. Finally, the damping matrix in the physical basis \mathbf{C} is computed. An ascending excitation is applied on the 149-th dof (located approximately at 0.75 m from the left end): $f(t) = 100 \cos(\omega t)$. The frequency range of interest $[0, 600]$ Hz embraces the first 3 modes of this 200 dofs model. Fig. 14 provides an overview of the system response variation over the frequency range of interest and shows that each of the three modes varies.

Two methods are used for total phase evaluation: full as defined by Eq. (11) and truncated with $N_\lambda = 5$ and a “static compensation” as defined by Eq. (41). This will demonstrate the accuracy of the truncated formula and provide elements for cost comparison of all the methods. As in the previous application

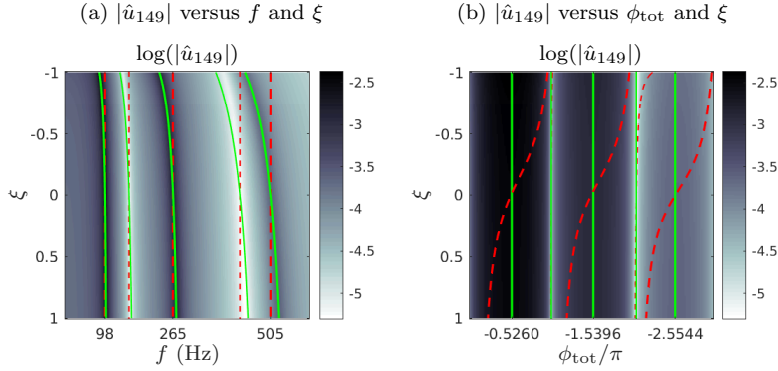


Figure 15: Beam, MCS – System 149-th dof response amplitude (\hat{u}_{149}) versus (a) f and ξ , (b) ϕ_{tot} and ξ . Dashed (red) lines: constant frequency paths; Solid (green) lines: constant total phase paths.

only amplitudes $|\hat{u}_k|$ (not angles) are approximated using polynomial chaos. Two dofs will be monitored: the displacement u_{149} where the force is applied and the displacement u_{101} of the node located approximately at 0.51 m of the left end of the beam.

Fig. 15 provides an overview of the system response variations by displaying dof 149 amplitude for various ξ values when evaluated using direct computation. Constant frequency and constant total phase lines are drawn for the first three resonances (thick lines) and the two anti-resonances (thin lines). This already shows that constant frequency lines cross responses with larger variations than constant total phase lines.

4.2.1. Accuracy

Fig. 16 displays relative error on mean and variance over the frequency range of interest in the CFA case (graphics (a) and (b)) and over the total phase range of interest in the CTPA case (graphics (c) and (d)). The grey patches match areas around resonances depicted in Fig. 17. These areas are defined as follows: for each ξ value in $\{-1, 0, +1\}$, the frf is computed over the whole frequency range and the maximum value over all translational displacements $|\hat{u}_{2k+1}|$ is stored for each frequency. Then, each resonance is located and frequencies or total phase matching neighbouring points with amplitude greater than half this resonance amplitude are used to define the areas.

Another way to evaluate the accuracy of the results is to use the Wasserstein distance [23, Chap. 6]. This distance provides a means to compare the quality of the approximation considering simultaneously the convergence on the mean, the variance and the distribution law.

The Wasserstein distance (Wd) of order 2 between two probability measures P_1 and P_2 having a second order moment is defined as [23]:

$$\text{Wd}_2(P_1, P_2) = \inf \left\{ \mathbb{E}[(X_1 - X_2)^2]^{1/2} : \mathcal{L}(X_1) = P_1, \mathcal{L}(X_2) = P_2 \right\}, \quad (46)$$

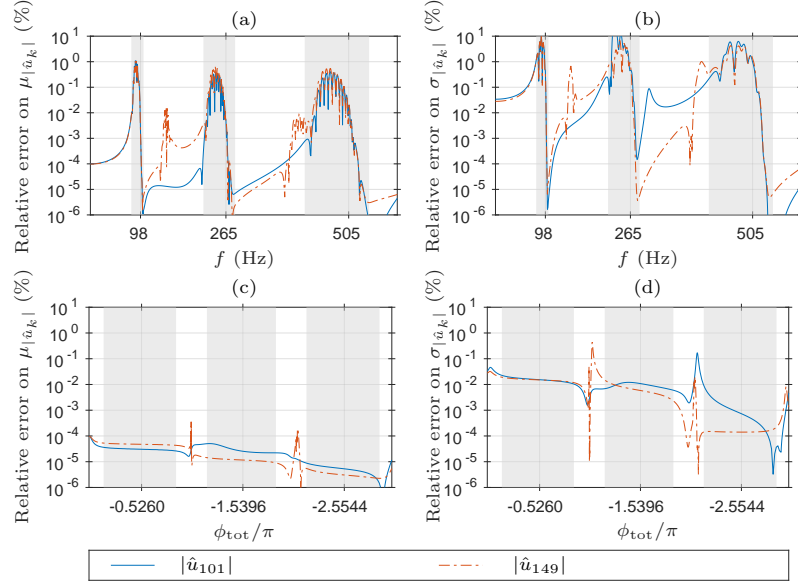


Figure 16: Beam, PCE, Accuracy comparison – Comparison of MCS and PCE results using global indicators over the full frequency range when using (a,b) CFA, (c,d) CTPA truncated with $N_\lambda = 5$. Relative error in percent for (a,c) mean and (b,d) standard deviation of $|\hat{u}_k|$. Solid line is relative to $|\hat{u}_{101}|$; dashed dotted line is relative to $|\hat{u}_{149}|$.

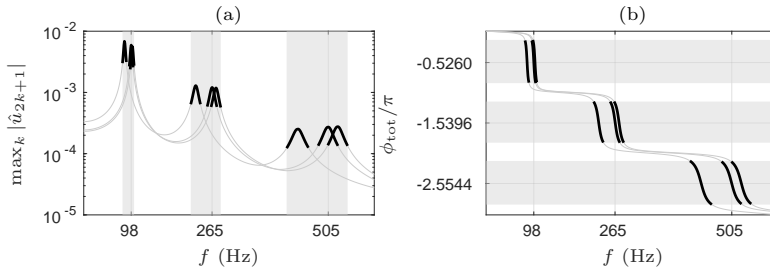


Figure 17: Beam, PCE, Accuracy comparison – Patches: Areas with amplitudes greater than half the resonance amplitude for (a) frequency and (b) total phase. Thin lines: realizations for $\xi \in \{-1, 0, +1\}$. Thick lines: portion of curves with amplitudes greater than half the resonance amplitude.

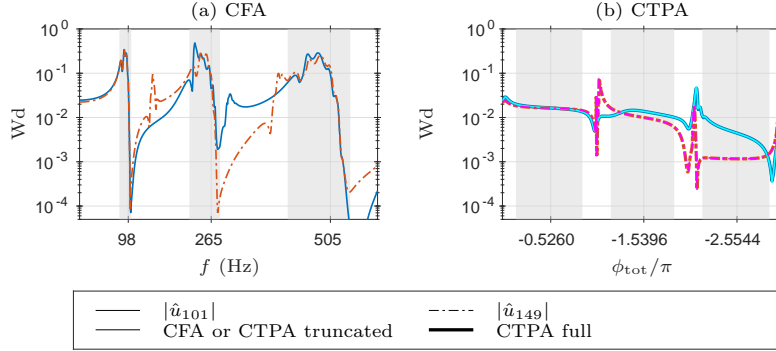


Figure 18: Beam, PCE, Accuracy comparison – Wasserstein distance for (a) CFA and (b) CTPA (full and truncated). Patches: Areas with amplitudes greater than half the resonance amplitude.

where $\mathcal{L}(X)$ denotes the law of X . It can be evaluated by:

$$\text{Wd}_2(P_1, P_2) = \left(\int_0^1 (F_{X_1}^{-1}(t) - F_{X_2}^{-1}(t))^2 dt \right)^{1/2}, \quad (47)$$

485 where F_X denotes the cumulative distribution function associated to X . The distance between the CFA or CTPA approximations and the reference sample U_{ref} can then be evaluated using Eq. (47). To render this distance dimensionless with respect to the order of magnitude of U [24], the Wasserstein distance of order 2 is divided by the standard deviation evaluated using the reference
 490 sample; this quantity is denoted Wd :

$$\text{Wd}(P_U, P_{U_{\text{ref}}}) = \left(\frac{\int_0^1 (F_U^{-1}(t) - F_{U_{\text{ref}}}^{-1}(t))^2 dt}{\sigma_{U_{\text{ref}}}^2} \right)^{1/2}. \quad (48)$$

These distances are plotted on Fig. 18 which shows that truncated and full CTPA methods provide the same accuracy and a greater accuracy than CFA. To get other illustrations of the Wasserstein distance in a mechanical frame, the reader is referred to [25, 26].

495 As in the previous application, the CFA suffer from higher errors around resonances while high errors in the case of CTPA are located in the vicinity of anti-resonances where amplitude get smaller. The lack of accuracy of CFA around resonances is illustrated in Fig. 19. CTPA results (using truncation with $N_\lambda = 5$) were used to rebuild the same constant frequency results according to Algorithm 3 and show better accuracy as depicted by Fig. 20. These results
 500 demonstrate the accuracy of CTPA even with a truncated evaluation when larger systems are studied.

Results in the vicinity of anti-resonances can be compared also. As both methods provide accurate results around the first anti-resonance ($f = 157$ Hz),
 505 only the second one is examined in Fig. 21. The left column displays the results

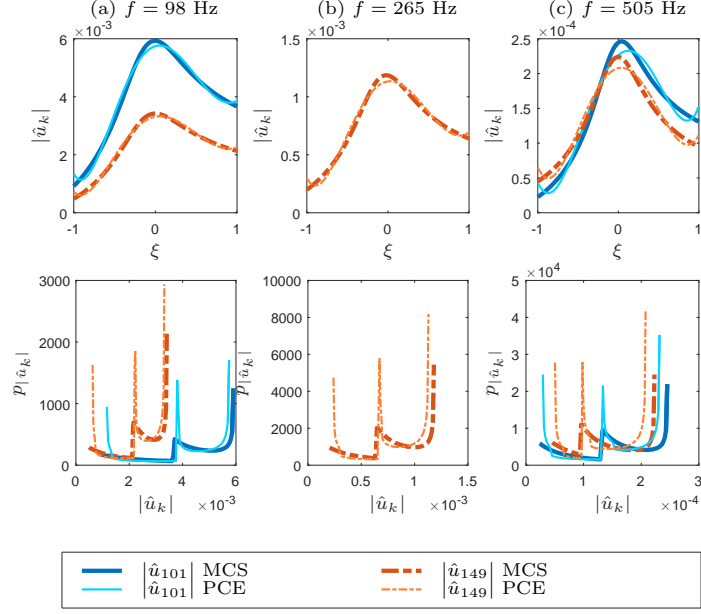


Figure 19: Beam, CFA – Comparison of MCS and PCE results for constant frequencies. Upper plots: $|\hat{u}_k|$ versus ξ ; lower plots: pdf of $|\hat{u}_k|$. $|\hat{u}_{101}|$ is not plotted in column (b) as its amplitude range is very low compared to $|\hat{u}_{149}|$.

obtained by CFA while the right column displays results obtained by CTPA with $N_\lambda = 5$ and using the constant frequency rebuild process from Sec. 2.3. This shows that the CTPA method which is designed to provide a greater accuracy around resonances is able to provide accurate results around anti-resonances too.

510

4.2.2. Numerical cost

No proper study with multiple runs was conducted. CPU times provided are hence given for guidance only. 601 $\omega^{(j)}$ values over $[0, 600 \times 2\pi]$ and 601 $\phi_{\text{tot}}^{(j)}$ values between $[-3.0298\pi, 0]$ were used. As a Gauss-Legendre quadrature rule with 11 nodes is used to evaluate PCE coefficients, each problem (17) or (18) has to be solved for 11 different $\xi_{\text{GL}}^{(i)}$ values. In the case of CTPA the constraint equation requires a numerical resolution and, for each $\xi_{\text{GL}}^{(i)}$ value, the $2 \times N_\lambda = 10$ smallest eigenvalues (if truncated) or all of them (if not truncated) have to be evaluated. MCS were run using 10001 ξ values in the sample.

515

520

Time for MCS is about 4 h for CFA, and 5 h 30 min for CTPA (+37.5%). Most of the additional time is due to the total phase function creation which implies computing \mathbf{L}_K and \mathbf{L}_M matrices for energy phase space linearisation and evaluating eigenvalues. Resolution of the nonlinear constraint equation using Matlab `fzero` function only accounts for about 3% of this additional time.

525

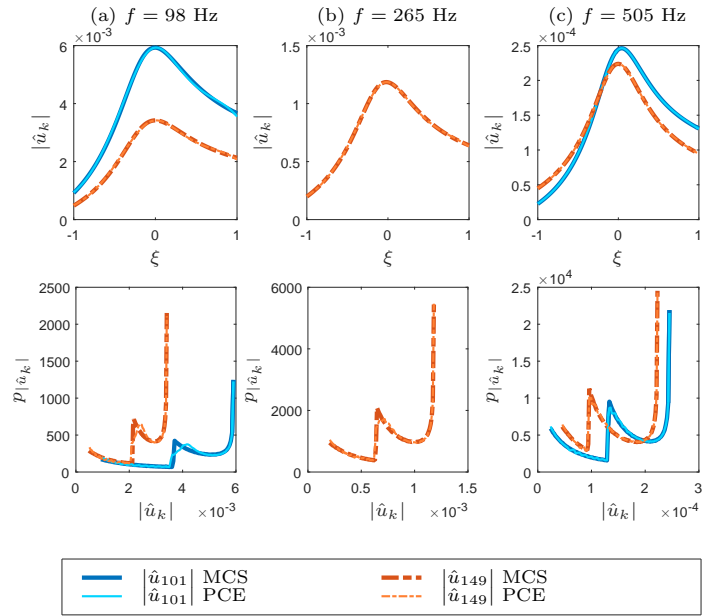


Figure 20: Beam, Constant frequency results rebuilt from CTPA truncated with $N_\lambda = 5$ – Comparison of MCS and PCE results for constant frequencies. Upper plots: $|\hat{u}_k|$ versus ξ ; lower plots: pdf of $|\hat{u}_k|$. $|\hat{u}_{101}|$ is not plotted in column (b) as its amplitude range is very low compared to $|\hat{u}_{149}|$.

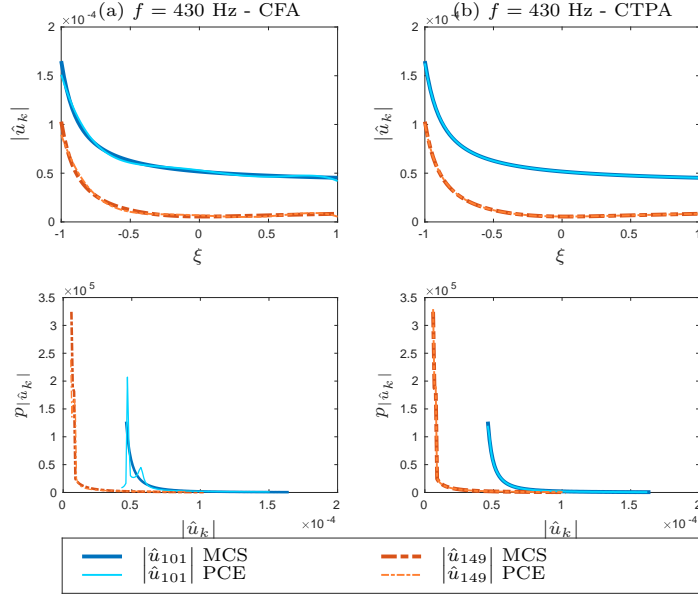


Figure 21: Beam – Comparison of MCS and PCE results around the second anti-resonance ($f = 430$ Hz). Upper plots: $|\hat{u}_k|$ versus ξ ; lower plots: pdf of $|\hat{u}_k|$. (a) Results from CFA; (b) Results rebuilt from CTPA truncated with $N_\lambda = 5$.

Time for PCE is about 15.5 s for CFA, 22.3 s for CTPA without truncation (+43.9%) and 21.5 s for CTPA truncated with $N_\lambda = 5$ (+38.7%). The gain of evaluating only some of the eigenvalues is not important as expected considering Fig. 2; however, it would increase for larger systems. If CTPA implies higher costs than CFA, it must be kept in mind that it returns accurate results and is more than 600 times cheaper than a MCS. The time to rebuild the three constant frequency plots in Fig. 20 from CTPA result is about 0.9 s.

5. Conclusions

A new parametrization of linear dynamical problems is proposed for systems with sub-critical damping. It uses a total phase parameter which involves the eigenvalues of the damped problem. It is demonstrated that one and only one dynamical solution (couple frequency/displacements) is associated to any value of this parameter. Stochastic dynamic responses are hence computed using given values for this total phase parameter rather than using given values for the frequency.

Two examples show that Polynomial Chaos Expansion with low degree then provides accurate results even in the vicinity of resonances that is where it usually loses accuracy when considering given frequency values. These illustrations show that the proposed parametrization gathers similar responses contrarily to

545 classical constant frequency parametrization which embraces very different dynamical responses.

Even though the current examples involve only one random variable, they prove that low degree PCE provide accurate results because the response variations are simpler to describe when considering a given total phase value rather than
550 a constant frequency value. Hence, in the case when multiple random variables are involved, the “curse of dimensionality” the PCE method suffers from will be limited as fewer monomial will have to be considered.

The limits of the method are not explored here. Further work should test it on systems for which modes switch for different realizations which can happen
555 when considering rotating machineries for example. One can guess that in this case, the accuracy will not be as good as for the systems tested in this paper and that some improvements should be developed. The case when some modes are over-damped, should be examined too. If high frequency over-damped modes should not be a problem for low frequency studies, the case when low frequency
560 modes do not respect the subcritical damping rule could be more difficult to handle.

References

- [1] L. Pichler, H. Pradlwarter, G. Schuller, A mode-based meta-model for the frequency response functions of uncertain structural systems, *Computers & Structures* 87 (5) (2009) 332 – 341, doi:[10.1016/j.compstruc.2008.12.013](https://doi.org/10.1016/j.compstruc.2008.12.013).
565
- [2] J. Wang, C. Wang, J. Zhao, Frequency response function-based model updating using Kriging model, *Mechanical Systems and Signal Processing* 87 (2017) 218 – 228, doi:[10.1016/j.ymssp.2016.10.023](https://doi.org/10.1016/j.ymssp.2016.10.023).
- [3] D. Xiu, G. E. Karniadakis, The Wiener–Askey Polynomial Chaos for Stochastic Differential Equations, *SIAM Journal on Scientific Computing* 24 (2) (2002) 619–644, doi:[10.1137/S1064827501387826](https://doi.org/10.1137/S1064827501387826).
570
- [4] E. Pagnacco, E. Sarrouy, R. Sampaio, E. Souza de Cursi, Polynomial chaos for modeling multimodal dynamical systems – Investigations on a single degree of freedom system, in: C. G. García Garino, A. E. Mirasso, M. A. Storti, M. E. Tornello (Eds.), *Mecánica Computacional, Proceeding of XX Congress on Numerical Methods and their Applications*, vol. XXXII, Mendoza, Argentina, 705–727, URL <http://www.cimec.org.ar/ojs/index.php/mc/article/view/4385/4315>, november 19-22, 2013.
575
- [5] J.-J. Sinou, E. Jacquelin, Influence of Polynomial Chaos expansion order on an uncertain asymmetric rotor system response, *Mechanical Systems and Signal Processing* 50 – 51 (2015) 718 – 731, doi:[10.1016/j.ymssp.2014.05.046](https://doi.org/10.1016/j.ymssp.2014.05.046).
580
- [6] E. Jacquelin, S. Adhikari, J.-J. Sinou, M. Friswell, Polynomial Chaos Expansion and Steady-State Response of a Class of Random Dynamical

- 585 Systems, *Journal of Engineering Mechanics* 141 (4) (2015) 04014145, doi:
[10.1061/\(ASCE\)EM.1943-7889.0000856](https://doi.org/10.1061/(ASCE)EM.1943-7889.0000856).
- [7] E. Jacquelin, S. Adhikari, J.-J. Sinou, M. I. Friswell, Polynomial chaos expansion in structural dynamics: accelerating the convergence of the first two statistical moment sequences, *Journal of Sound and Vibration* 356
 590 (2015) 144–154, doi:[10.1016/j.jsv.2015.06.039](https://doi.org/10.1016/j.jsv.2015.06.039).
- [8] X. Wan, G. Karniadakis, Multi-element generalized polynomial chaos for arbitrary probability measures, *SIAM Journal on Scientific Computing* 28 (2006) 901–928, doi:[10.1137/050627630](https://doi.org/10.1137/050627630).
- [9] E. Sarrouy, E. Pagnacco, E. S. de Cursi, A constant phase approach for the frequency response of stochastic linear oscillators, *Mechanics & Industry*
 595 17 (2) (2016) 206, doi:[10.1051/meca/2015057](https://doi.org/10.1051/meca/2015057).
- [10] V. Yaghoubi, S. Marelli, B. Sudret, T. Abrahamsson, Sparse polynomial chaos expansions of frequency response functions using stochastic frequency transformation, *Probabilistic Engineering Mechanics* 48 (2017) 39 – 58,
 600 ISSN 0266-8920, doi:[10.1016/j.probengmech.2017.04.003](https://doi.org/10.1016/j.probengmech.2017.04.003).
- [11] M. Loève, *Probability Theory II*, Springer-Verlag, 1978.
- [12] A. Papoulis, S. Pillai, *Probability, Random Variables, and Stochastic Processes*, McGraw-Hill series in electrical engineering: Communications and signal processing, McGraw-Hill, ISBN 9780070486584, 2002.
- 605 [13] D. Lucor, G. E. Karniadakis, Adaptive Generalized Polynomial Chaos for Nonlinear Random Oscillators, *SIAM Journal on Scientific Computing* 26 (2) (2004) 720–735, doi:[10.1137/S1064827503427984](https://doi.org/10.1137/S1064827503427984).
- [14] O. G. Ernst, A. Mugler, H.-J. Starkloff, E. Ullmann, On the convergence of generalized polynomial chaos expansions, *ESAIM: Mathematical Modelling and Numerical Analysis* 46 (2012) 317–339, doi:[10.1051/m2an/2011045](https://doi.org/10.1051/m2an/2011045).
 610
- [15] T. K. Caughey, M. E. J. O’Kelly, Classical Normal Modes in Damped Linear Dynamic Systems, *Journal of Applied Mechanics* 32 (3) (1965) 583–588, doi:[10.1115/1.3627262](https://doi.org/10.1115/1.3627262).
- 615 [16] F. Tisseur, K. Meerbergen, The Quadratic Eigenvalue Problem, *SIAM Review* 43 (2) (2001) pp. 235–286, doi:[10.1137/S0036144500381988](https://doi.org/10.1137/S0036144500381988).
- [17] K. Veselić, *Damped Oscillations of Linear Systems: A Mathematical Introduction*, Springer-Verlag Berlin Heidelberg, doi:[10.1007/978-3-642-21335-9](https://doi.org/10.1007/978-3-642-21335-9), 2011.
- 620 [18] F. Ma, A. Imam, M. Morzfeld, The decoupling of damped linear systems in oscillatory free vibration, *Journal of Sound and Vibration* 324 (12) (2009) 408 – 428, doi:[10.1016/j.jsv.2009.02.005](https://doi.org/10.1016/j.jsv.2009.02.005).

- [19] D. Xiu, Numerical Methods for Stochastic Computations – A Spectral Method Approach, Princeton University Press, 2010.
- [20] W. Duncan, A. Collar, Matrices applied to the motions of damped systems, The London, Edinburgh, and Dublin Philosophical Magazine and Journal of Science 19 (125) (1935) 197–219, doi:[10.1080/14786443508561366](https://doi.org/10.1080/14786443508561366).
- [21] Y. Saad, Numerical methods for large eigenvalue problems, SIAM, doi:[10.1137/1.9781611970739](https://doi.org/10.1137/1.9781611970739), 2011.
- [22] D. Afolabi, Linearization of the quadratic eigenvalue problem, Computers & Structures 26 (6) (1987) 1039 – 1040, doi:[10.1016/0045-7949\(87\)90120-9](https://doi.org/10.1016/0045-7949(87)90120-9).
- [23] C. Villani, Optimal transport. Old and new, vol. 338 of *Grundlehren der mathematischen Wissenschaften*, Springer-Verlag, Berlin, doi:[10.1007/978-3-540-71050-9](https://doi.org/10.1007/978-3-540-71050-9), 2009.
- [24] E. del Barrio, J. A. Cuesta-Albertos, C. Matrán, J. M. Rodríguez-Rodríguez, Tests of goodness of fit based on the L_2 -Wasserstein distance, Ann. Statist. 27 (4) (1999) 1230–1239, doi:[10.1214/aos/1017938923](https://doi.org/10.1214/aos/1017938923).
- [25] B. Chouvion, E. Sarrouy, Development of error criteria for adaptive multi-element polynomial chaos approaches, Mechanical Systems and Signal Processing 66–67 (2016) 201 – 222, ISSN 0888-3270, doi:[10.1016/j.ymsp.2015.05.007](https://doi.org/10.1016/j.ymsp.2015.05.007).
- [26] E. Pagnacco, E. Sarrouy, R. Sampaio, E. Souza de Cursi, Pitfalls in the frequency response represented onto polynomial chaos for random SDOF mechanical systems, Applied Mathematical Modelling 52 (2017) 626–647, doi:[10.1016/j.apm.2017.08.004](https://doi.org/10.1016/j.apm.2017.08.004).

Appendix A. Evaluating the response using a complex rewriting of the dynamical equation

Injecting excitation and amplitude decompositions (2) and (3) into the dynamical equation (1) and balancing cosine and sine terms, one gets 2 real equations with size n :

$$(\mathbf{K} - \omega^2 \mathbf{M})\mathbf{a} + \omega \mathbf{C}\mathbf{b} = \mathbf{f}^c \quad (\text{A.1a})$$

$$(\mathbf{K} - \omega^2 \mathbf{M})\mathbf{b} - \omega \mathbf{C}\mathbf{a} = \mathbf{f}^s \quad (\text{A.1b})$$

To compute \mathbf{a} and \mathbf{b} , one can either solve this linear system with size $2n$ or consider the following composition in the complex space \mathbb{C}^n , (A.1a) – j (A.1b):

$$\underbrace{(\mathbf{K} - \omega^2 \mathbf{M} + j\omega \mathbf{C})}_{\hat{\mathbf{K}}(\omega)} \underbrace{(\mathbf{a} - j\mathbf{b})}_{\hat{\mathbf{u}}} = \underbrace{(\mathbf{f}^c - j\mathbf{f}^s)}_{\hat{\mathbf{f}}} \quad (\text{A.2})$$

By analogy with the static case ($\omega = 0$), $\hat{\mathbf{K}}(\omega)$ is often called the dynamic stiffness matrix and its inverse, denoted $\hat{\mathbf{S}}(\omega)$ the dynamical flexibility matrix.

Appendix B. Demonstration of equation (40)

Case of a classical linearisation (32). The first step is to express the inverse of matrix \mathbf{A} defined in Eq. (32). Since \mathbf{K} is supposed to be symmetric definite positive, it is invertible and one can write

$$\mathbf{A}^{-1} = \begin{bmatrix} \mathbf{K}^{-1}\mathbf{C}\mathbf{U}^{-1} & \mathbf{K}^{-1} \\ -\mathbf{U}^{-1} & \mathbf{0} \end{bmatrix} \quad (\text{B.1})$$

655 whatever \mathbf{U} matrix is, provided it is invertible. The next step is to note that since λ_k are the eigenvalues of the linear eigenvalue problem associated to Eq. (32):

$$\text{tr}(\mathbf{A}^{-1}\mathbf{B}) = -\sum_{k=1}^{2n} \frac{1}{\lambda_k} \quad (\text{B.2})$$

Finally the detailed expression of $\mathbf{A}^{-1}\mathbf{B}$,

$$\mathbf{A}^{-1}\mathbf{B} = \begin{bmatrix} \mathbf{K}^{-1}\mathbf{C} & \mathbf{K}^{-1}\mathbf{M} \\ -\mathbf{I} & \mathbf{0} \end{bmatrix} \quad (\text{B.3})$$

leads to the expected result

$$\text{tr}(\mathbf{A}^{-1}\mathbf{B}) = \text{tr}(\mathbf{K}^{-1}\mathbf{C}) = -\sum_{k=1}^{2n} \frac{1}{\lambda_k} \quad (\text{B.4})$$

660 *Case of an energy phase space linearisation (36).* In this second case, only one matrix \mathbf{A}_e is involved. Its inverse is:

$$\mathbf{A}_e^{-1} = \begin{bmatrix} -\mathbf{L}_K^{-1}\mathbf{C}\mathbf{L}_K^{-\text{T}} & -\mathbf{L}_K^{-1}\mathbf{L}_M \\ \mathbf{L}_M^{\text{T}}\mathbf{L}_K^{-\text{T}} & \mathbf{0} \end{bmatrix} \quad (\text{B.5})$$

The result is straightforward:

$$\text{tr}(\mathbf{A}_e^{-1}) = \text{tr}(-\mathbf{L}_K^{-1}\mathbf{C}\mathbf{L}_K^{-\text{T}}) = \sum_{k=1}^{2n} \frac{1}{\lambda_k} \quad (\text{B.6})$$

Appendix C. Phase sampling

The method to create samples of total phase values for which system response
 665 should be evaluated is not obvious. Indeed, using equally spaced values would not return a relevant mesh of the dynamic response as illustrated via Fig. C.22. The good point of an equally spaced total phase sample is that it focuses on the resonance peaks; the bad point is that there is not enough points in between these ranges. On the contrary, an equally spaced frequency sample does not
 670 focus on resonance peaks and can somehow miss them but describes ranges outside resonances more properly. A mix is then proposed to build an efficient total phase sampling: a linear spacing of total phase values is used around

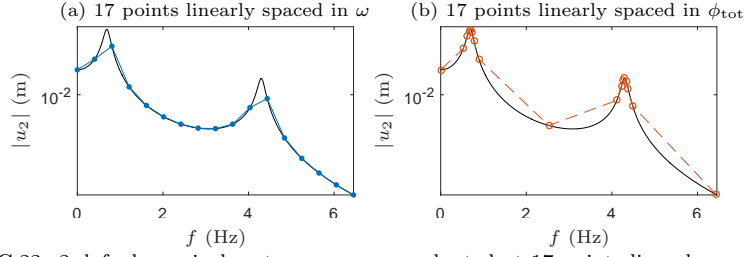


Figure C.22: 2-dofs dynamical system response evaluated at 17 points linearly spaced (a) in frequency and (b) in total phase.

resonances and a spacing such that one gets an approximate linear spacing in frequencies in between these ranges.

675 Let's assume that one wants to study the response of a structure over its first K modes included in $[0, \omega_{\max}]$ range for circular frequency. The equivalent range in total phase is $[\phi_{\text{tot max}}, 0]$ where $\phi_{\text{tot max}}$ is evaluated from Eq. (11) or Eq. (41) and ω_{\max} . First, one has to define ranges around resonances: resonance for mode k occurs when the k -th partial total phase factor $\phi_{\text{tot},k}$ is close to $-\pi/2$.
 680 Let's define the limits around $-\pi/2$ for which most of the resonance peak is embraced: $\phi_{\text{lim}}^- = -\pi/10$ and $\phi_{\text{lim}}^+ = -9\pi/10$. ω_k^- and ω_k^+ such that $\phi_{\text{tot},k}(\omega_k^\pm) = \phi_{\text{lim}}^\pm$ can be computed from these values, using Eq. (12). This is illustrated in Fig. C.23(a). Corresponding total phase limit values $\phi_{\text{tot } k}^\pm$ can then be easily computed using either Eq. (11) or Eq. (41). This is illustrated via Fig. C.23(b). Finally, this let us define the following zones:

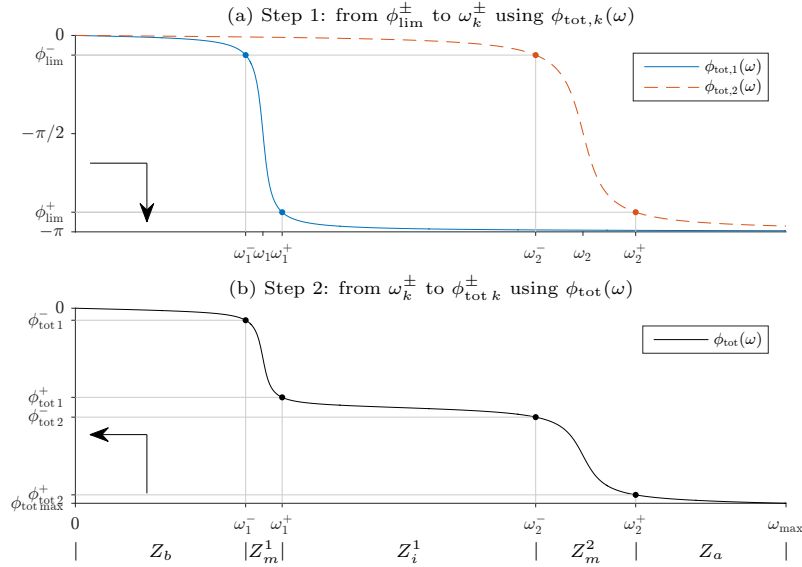


Figure C.23: Sampling zones definition

685

- Z_b : zone before the first resonance. $\omega \in [0, \omega_1^-]$ and $\phi_{\text{tot}} \in [\phi_1^-, 0]$.
- Z_m^k : zone around the k -th resonance. $\omega \in [\omega_k^-, \omega_k^+]$ and $\phi_{\text{tot}} \in [\phi_k^+, \phi_k^-]$.
- Z_i^k : intermediate zone between the k -th and $(k+1)$ -th resonances. $\omega \in [\omega_k^+, \omega_{k+1}^-]$ and $\phi_{\text{tot}} \in [\phi_{k+1}^-, \phi_k^+]$.
- 690 • Z_a : zone after the last resonance. $\omega \in [\omega_K^+, \omega_{\text{max}}]$ and $\phi_{\text{tot}} \in [\phi_K^+, \phi_{\text{tot max}}]$.

In zones Z_m^k , total phase points are equally spaced in total phase; in zones Z_b , Z_i^k and Z_a , total phase sampling is such that points are equally spaced in frequency (this is done by computing images of linearly spaced samples in ω using either Eq. (11) or Eq. (41)).

700 The last thing to determine is the ratio of points in each zone. These ratios are up to the user and may vary from one study to another. The ratios used throughout the paper are 25% for Z_m^k zones, and the other 75% are distributed such that Z_b and Z_a are described with the same number of points and each Z_i^k zone has twice the number of points of Z_b zone. The resulting percentage of points in each zone for $K = 2$ and $K = 3$ modes are provided in Tab. C.1.

Zone	Z_b	Z_m^k	Z_i^k	Z_a
$K = 2$	18.75%	12.5%	37.5%	18.75%
$K = 3$	12.5%	8.333%	25%	12.5%

Table C.1: Percentage of points in each zone for K modes.

700 To illustrate the interest of such a phase sampling, dynamic responses of the two systems used for applications in Sec. 4 are computed using either linearly spaced values in frequency (as is usually done) and total phase samples computed as explained above, using the same number of points in both samples.

705 The error in the rebuilt responses is evaluated for one dof by the integral of the absolute difference between the resulting curve and a reference curve obtained via a very fine sampling in frequency (area between both curves). Results are displayed on Fig. C.24 and Fig. C.25. As expected, considering a same number of points N , the resonance peaks are described more accurately using the

710 proposed total phase sampling method while keeping enough points in between these areas. Moreover, the error with a reference curve is very much smaller in the general case which indicates that it may be interesting to use such a sampling to compute frf with a minimal number of points even in the deterministic case.

715 Appendix D. 2-dof system with a Gaussian random variable

The 2-dof system illustrated in Sec. 4.1 is considered but with a deterministic k_1 value and a random k_2 variable which follows a normal law:

$$\tilde{k}_2 = k_2(1 + \xi \Delta k_2) \quad (\text{D.1})$$

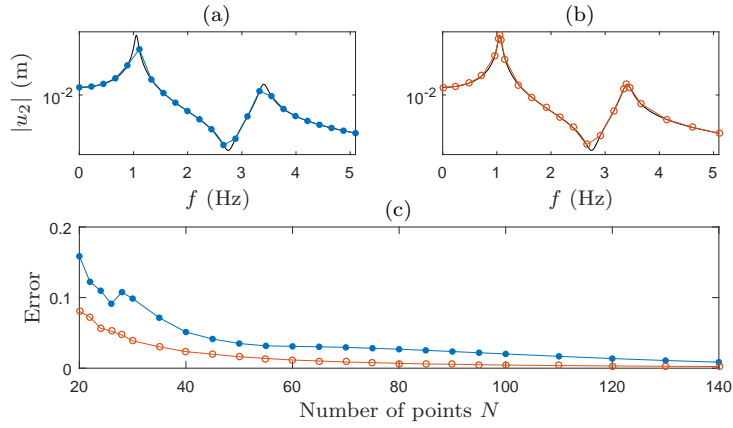


Figure C.24: Total phase sampling efficiency - 2-dofs system of Sec. 4.1, amplitude for dof 2 for 24 points (a) linearly spaced in frequency and (b) spaced in total phase as proposed; (c) Value of error between a reference frf and a frf with N points ($\text{---}\bullet\text{---}$) linearly spaced in frequency or ($\text{---}\circ\text{---}$) computed using the proposed total phase sampling scheme.

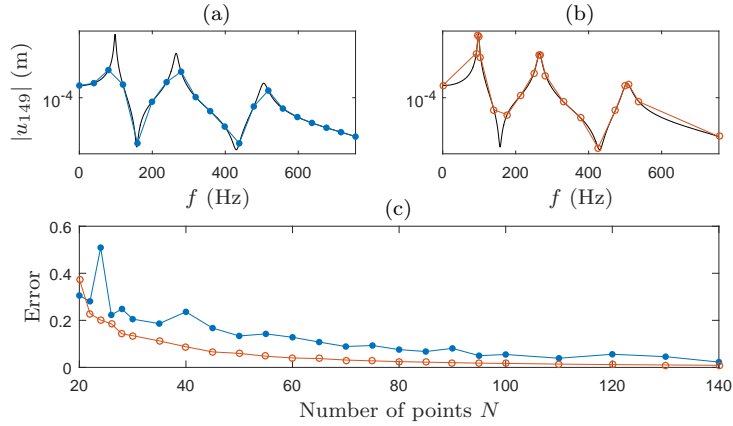


Figure C.25: Total phase sampling efficiency - Beam of Sec. 4.2, amplitude for dof 149 for 20 points (a) linearly spaced in frequency and (b) spaced in total phase as proposed; (c) Value of error between a reference frf and a frf with N points ($\text{---}\bullet\text{---}$) linearly spaced in frequency or ($\text{---}\circ\text{---}$) computed using the proposed total phase sampling scheme.

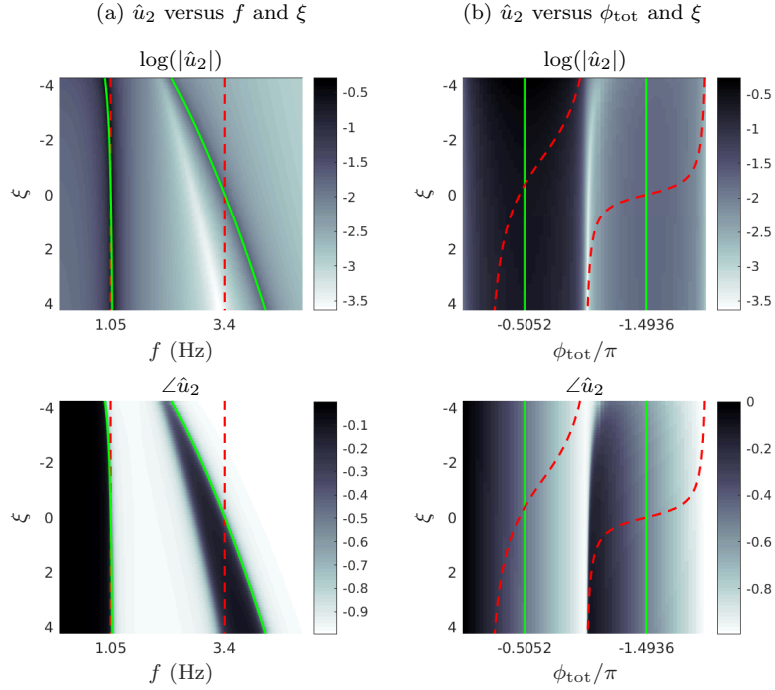


Figure D.26: 2-dofs Gaussian, MCS – System second dof response (\hat{u}_2) versus (a) f and ξ , (b) ϕ_{tot} and ξ . Dashed (red) lines: constant frequency paths; Solid (green) lines: constant total phase paths.

with $\Delta k_2 = 0.15$ and $\xi \sim \mathcal{N}(0, 1)$. ξ realizations leading to negative stiffness are put aside. The computations are the same than in Sec. 4.1 except that a Hermite polynomial basis is used for PCE (still with degree 5).

This configuration leads to an almost constant first mode but a second mode with large variations as depicted in Fig. D.26. This figure shows again that while constant frequency cuts account for very different responses for the second mode, constant total phase cuts gather very similar responses. Hence, the response approximation by PCE is more accurate when considering CTPA than CFA. This is illustrated in Fig. D.27 which shows the results obtained considering a constant frequency cut around the second mode. While the direct degree 5 polynomial approximation of \hat{u}_2 in the case of CFA presents high errors leading to erroneous pdfs (column (a)), the degree 5 approximations in the CTPA case have good enough accuracies which provide a mean to rebuild a very accurate constant frequency response (column (b)) using the steps explained in Sec. 2.3.

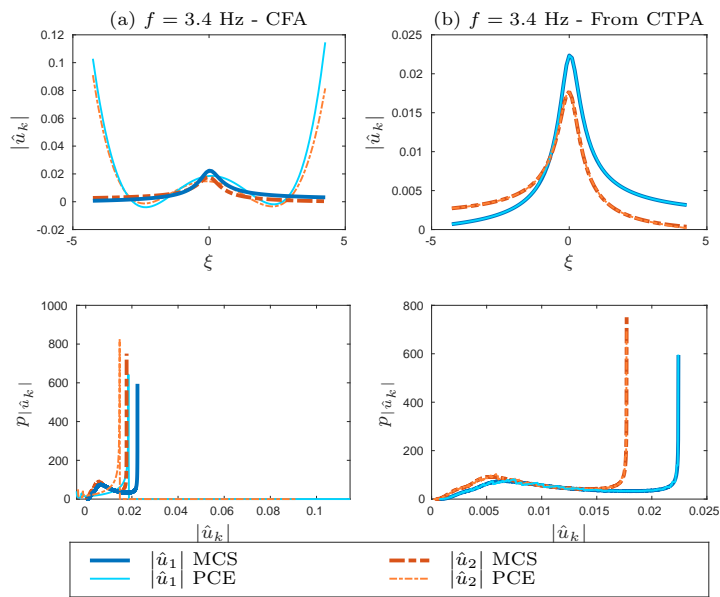


Figure D.27: 2-dofs Gaussian – Comparison of MCS and PCE results around the second mode ($f = 3.4$ Hz). Upper plots: $|\hat{u}_k|$ versus ξ ; lower plots: pdf of $|\hat{u}_k|$. (a) Results from CFA; (b) Results rebuilt from CTPA.